Computers and Structures 321 (2026) 108079

Contents lists available at ScienceDirect

Computers and Structures

journal homepage: www.elsevier.com/locate/compstruc

A new concrete material model embedded in finite element procedures

Yeongbin Ko [a,*], Klaus-Jürgen Bathe [b]

[a] Bentley Systems, incorporated, Team ADINA, 685 Stockton Drive, Exton, PA 19341, USA
[b] Department of Mechanical Engineering, Massachusetts Institute of Technology, Cambridge, MA 02139, USA

ARTICLE INFO

Keywords:
Concrete
Finite element method
Compression coordinate system
Different failure surfaces
Coupling of plasticity and fracture
Nonlinear solution procedure

ABSTRACT

We present a new strain-based concrete material model that is generally applicable in two- and three-dimensional finite element analyses. The relevant constitutive laws are derived from a theory of plasticity and fracture for concrete, and the nonlinear solution process is described. The nonlinear behavior of the concrete includes crushing, crack opening and closing. The model is based on the use of the principal elastic strain directions and a "compression coordinate system" using different failure surfaces for the different "directions" in that system. The plastic-fracturing behavior is represented by a coupling between the plasticity and fracture in the finite element solution. The predictability and performance of the new material model, used with the finite element procedures, is evaluated and compared with results obtained in physical experiments and benchmark problems.

1. Introduction

While finite element analyses are already widely performed, the analysis of concrete structures with models of concrete materials still represents significant difficulties. Concrete materials undergo complex mechanisms involving nonlinear compression, fracture and cracking, and these different characteristics of behavior interact to possibly cause an overall failure of a structure. The finite element solution representing the behavior of concrete should be accurate in correctly representing measured experimental behavior, as well as be stable and show good convergence in nonlinear analyses. These properties can only be reached with an accurate constitutive law which needs to be implemented effectively. Because of the importance of using an accurate and effective finite element representation of concrete structures, research efforts have been expended on this task already for about half a century [1–5].

For the analysis of concrete behavior with softening, notably two frameworks have been developed: namely, the plastic-fracturing theory [6,7] and the damaged plasticity [8]. The plastic-fracturing theory combines incremental plasticity and microcracking theories to obtain general differential relations on stress, strain, and internal plastic strains. The damaged plasticity combines concepts of plasticity and damage mechanics, and the softening behavior is represented with the damage variable. Both frameworks can include micro-plane [9–13] and lattice models [14,15] of concrete.

Although many research advances have been accomplished in material models, not many material models are applicable to finite element analysis. Many material models and their frameworks involve stress quantities as unknowns to be solved [6,7,16], whereas the governing unknowns in a finite element analysis are displacements and strains. Another major challenge is the difficulty in obtaining a multi-dimensional constitutive law applicable to a multi-dimensional continuum, due to rational and non-polynomial functions describing material behavior [17–20]. The underlying reason is that complex concrete behavior naturally involves rational forms of stress [6] to include failure, including softening, in terms of general plastic-fracturing theory.

There are further valuable approaches for modeling fracture of cracks and regularizing the behaviors, including non-local models, gradient plasticity, and phase-field models, which sometimes occur in conjunction with a damaged plasticity model. Non-local models utilize strains at integration points that are averaged across different cells outside the finite element [21–23]. Gradient models require the interpolation of a separate gradient field in addition to the element's displacement field [23–27]. Our aim is to develop a strategy that utilizes the generic displacement-based finite element procedure as it is, without requiring special modifications for specific material behaviors. Additionally, phase-field models interpolate cracks using a continuous phase variable [28,29]. Although these approaches are accurate, they necessitate solving separate interpolation fields. Therefore, we focus on standard methods to address crack behavior and their regularization [22,30,31] based on smeared crack [31] and crack band approaches

---

* Corresponding author.
E-mail address: Yeongbin.Ko@bentley.com (Y. Ko).

https://doi.org/10.1016/j.compstruc.2025.108079
Received 7 August 2025; Accepted 15 December 2025

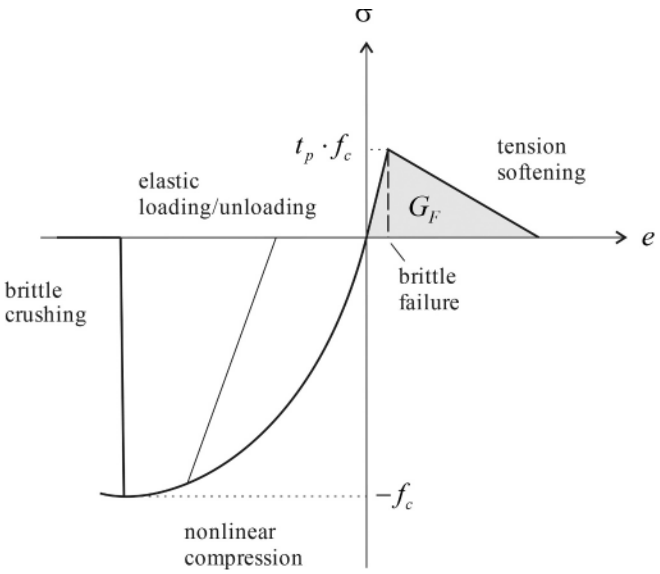

Fig. 1. Behavior classification of concrete. (f_c compressive strength of concrete, t_p the tensile to compressive strength ratio, G_F fracture energy per unit crack surface).

[30].

There have been research efforts in obtaining a general solution scheme, such as given by MD Kotsovos and MN Pavlović [31] and J Červenka and VK Papanikolaou [32]. MD Kotsovos proposed the finite element solution with experimental moduli as a fracturing step. J Červenka provided a finite element solution analysis framework for the multi-surface plasticity utilizing several return mapping steps [32]. However, the use of a fracturing step alone would not pass the test of ultimate strength, and the method to use at a minimum the plasticity steps [33] from the plastic-fracturing framework is still missing.

In the present paper, we build upon the ideas of previous researchers on modeling concrete materials to arrive at a new simple and generally applicable model based on plasticity and fracture for general finite element analyses. The new solution procedure is based on a theory involving plasticity and fracture of the concrete material using two coordinate systems, namely the 'principal system of the elastic strains' and the 'compression system' of the material compression. These coordinate systems are modified from earlier works [16–18,31] and employed simultaneously and effectively in the finite element solution procedure [33].

In the following sections we first describe and discuss the new model of concrete with an emphasis on modeling the physical behaviors, then derive the governing equations of the model in three-dimensional actions and thereafter show how the model is "embedded" in the finite element solution process. The concrete model can be used with the traditional finite elements and also novel procedures as long as the constitutive relationship is only evaluated locally at the integration points [34–37]. We finally illustrate the validity and strength of the model and its finite element implementation by solving various physical problems of concrete structures and numerical benchmark problems taken from references.

2. Formulation of the material model

In this section we describe the theory used to represent the plastic and fracture behaviors of concrete in general three-dimensional stress conditions. We present how the model incorporates compression, crushing, tension, cracking with tension softening and briefly mention how the model includes reinforcement.

2.1. The new concrete model based on plasticity, fracture and tensile failure

Our objective is here to briefly summarize the phenomenological plastic-fracturing theory of concrete, with a view towards the behavior of concrete in compression, tension and cracking.

In three-dimensional analyses, the volumetric and deviatoric stresses and strains are given by

$$\sigma_{kk} = \sigma_{11} + \sigma_{22} + \sigma_{33}, \ \sigma_{ij}^{dev} = \sigma_{ij} - \delta_{ij}\sigma_{kk}/3, \tag{1a}$$

$$e_{kk} = e_{11} + e_{22} + e_{33}, \ e_{ij}^{dev} = e_{ij} - \delta_{ij}e_{kk}/3, \tag{1b}$$

where σ_{ij} and e_{ij} are the global Cartesian components of the stress and strain tensors in indicial notation and δ_{ij} is the Kronecker delta [34].

Concrete subjected to compression exhibits nonlinear behavior which can lead to failure, while the tensile behavior or cracking of concrete can be modeled using a judiciously applied linear material behavior, see Fig. 1.

Whether the material is in tension or compression is decided using

$$\sigma_o = \sigma_{kk}/3 = (\sigma_{11} + \sigma_{22} + \sigma_{33})/3$$

with the conditions

$$\begin{array}{l} \text{if}, \sigma_o \geqslant 0 \text{ then the material is in tension, and} \\ \text{if}, \sigma_o < 0 \text{ then the material is in compression} \end{array} \tag{2a}$$

Furthermore, we need to identify when the concrete material is entering the "loading" condition over the complete response calculation. This condition is identified using the J_2-invariant

$$\tau_o = \sqrt{\frac{2J_2}{3}} = \sqrt{\frac{\sigma_{ij}^{dev}\sigma_{ij}^{dev}}{3}}$$

$$\begin{array}{l} \text{if}, \tau_o > \tau_o^{\max} \text{ then the material is in loading, and} \\ \text{if}, \tau_o \leqslant \tau_o^{\max} \text{ then the material is in unloading} \end{array} \tag{2b}$$

where $\tau_o^{\max}$ is the maximum value of τ_o reached in the complete material history over the converged configurations to time t. In compressive loading, the material will reach a nonlinear behavior, see Fig. 1.

It is useful to see the overall aim of the Section 2.1 presentations that follow. In Sections 2.1.1 and 2.1.2, the physical assumptions in the theories of plasticity and fracture are reviewed, and a strain and stress decomposition is proposed to include the plasticity and fracture effects in finite element applications. These basic thoughts lead to reach in Section 2.1.3 and 2.1.4 a novel material model for use in finite element analysis. These presentations are followed, in Sections 2.1.5 and 2.1.6, to describe how crack evolutions are modeled and how steel reinforcement is included in the analysis.

2.1.1. The essence of modeling concrete using the theories of plasticity and fracture

We briefly review a framework of elastic–plastic-fracturing behavior, see also Refs. [6,7]. This framework is useful in modeling the concrete material behavior.

The formulation uses the following stresses and strains, in differential form,

$$de_{ij}^{dev} = \frac{d\sigma_{ij}^{dev}}{2G} + de_{ij}^{p,dev}, \ de_{kk} = \frac{d\sigma_{kk}}{3K} + de_{kk}^{p}, \tag{3a}$$

and

$$d\sigma_{ij}^{dev} = 2G de_{ij}^{dev} + d\sigma_{ij}^{f,dev}, \ d\sigma_{kk} = 3K de_{kk} + d\sigma_{kk}^{f}, \tag{3b}$$

$$d\sigma_{ij}^{f,dev} = 2e_{ij}^{dev} dG, \ d\sigma_{kk}^{f} = 3e_{kk} dK, \tag{3c}$$

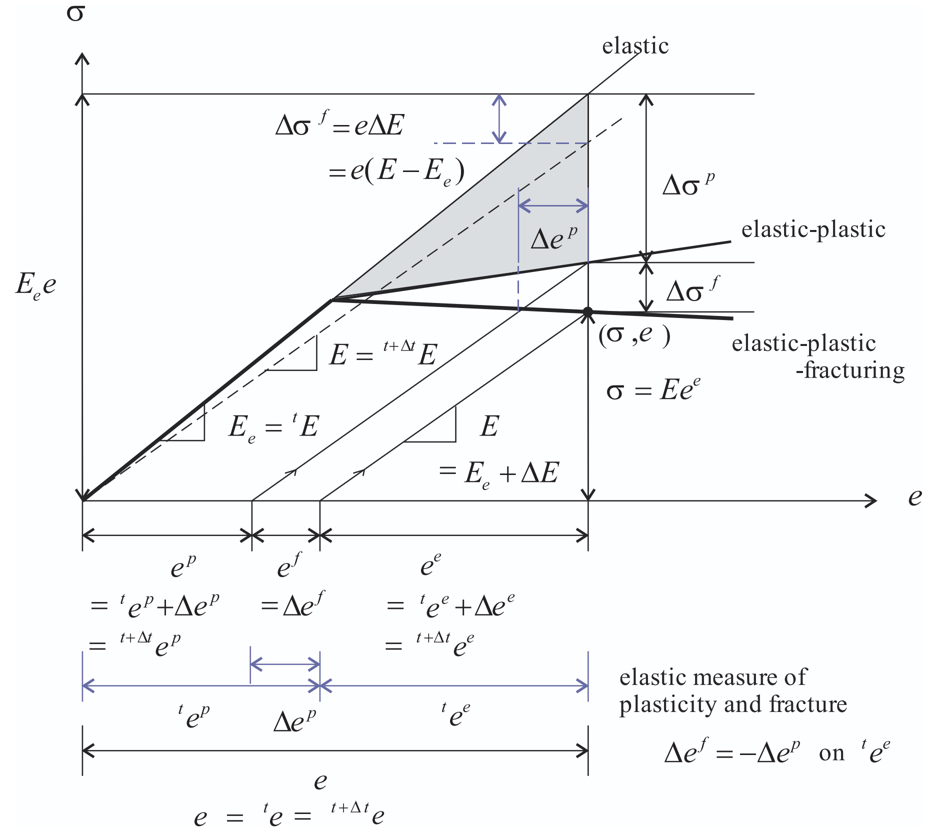

Fig. 2. Schematic framework of elasto-plasticity and fracture in 1D. The framework shows schematically the variables used in the concrete model.

where G and K are the shear and bulk moduli, and the superscripts e, p and f denote the elastic, plastic and fracture quantities.

For our conceptual study, we consider a one-dimensional (1D) condition and use finite increments rather than differential changes, see Fig. 2. Considering only plasticity we have

$$\Delta e = \frac{\Delta\sigma}{E} + \Delta e^{p}, \tag{4a}$$

and considering only the effects of fracture we have

$$\Delta\sigma = E\Delta e + \Delta\sigma^{f}, \tag{4b}$$

where

$$\Delta\sigma^{f} = e\Delta E. \tag{4c}$$

Here σ and e are the 1D total stress and strain, E is the instantaneous Young's modulus used to represent the physical behavior of our material model, and ΔE is the change in the Young's modulus.

One-dimensional case including plasticity and fracture

Empirically, we have the following form for the change of the Young's modulus

$$dE = -E\cdot\gamma\cdot e^{e} de^{e}, \ \gamma = \frac{E}{E_e}, \tag{5}$$

where E_e is the modulus of elasticity in the initial configuration and E is the current updated modulus. We note that E decreases as γ decreases, with $0 < \gamma < 1$. This decrease is a consequence of fracture as shown also in Fig. 2.

Considering the strains, we can decompose the total strain to obtain

$$\begin{aligned} e &= e^{e} + e^{p} + e^{f}, \\ e^{e} &= e - e^{p} - e^{f}, \\ \Delta e &= \Delta e^{e} + \Delta e^{p} + \Delta e^{f}, \end{aligned} \tag{6a}$$

where

$$\sigma = E e^{e}. \tag{6b}$$

The stress when measured on the strain assuming only elastic deformations decreases due to plasticity and also due to fracture, see Fig. 2.

In classical references, the equations regarding fracture and plasticity have largely been derived in terms of decomposing the stress, see e.g. [6,7], whereas we will use the strains as the primary drivers of the solution process.

Another important consideration is that for a finite element solution procedure to be applicable to a multi-dimensional continuum, the solution scheme best measures increments in a simple polynomial form [34,36], so that relevant derivatives can be defined without complexity.

2.1.2. *Decomposition of the elastic-fracturing and elastic–plastic effects*

We propose in this section how to measure elastic-fracturing and elasto-plasticity in a multiple-dimensional behavior.

Three-dimensional idealization

Consider the three-dimensional (3D) system 1, 2, 3, in which the strains (e_1^{e}, e_2^{e}, e_3^{e}) and stresses (σ_1, σ_2, σ_3) are defined with the canonical dependence relations to invariants,

$$\begin{aligned} &D_1 = e^{e}_{ij}\delta_{ij},\ D_2 = e^{e,dev}_{ij}e^{e,dev}_{ji}/2,\ D_3 = e^{e,dev}_{ij}e^{e,dev}_{jk}e^{e,dev}_{ki}/3, \\ &\quad I_1 = \sigma_{ij}\delta_{ij},\ J_2 = \sigma^{dev}_{ij}\sigma^{dev}_{ji}/2,\ J_3 = \sigma^{dev}_{ij}\sigma^{dev}_{jk}\sigma^{dev}_{ki}/3, \end{aligned} \tag{7a}$$

$$\begin{aligned} &\sigma_1 = \sigma_1(I_1),\ \sigma_2 = \sigma_2(J_2, J_3),\ \sigma_3 = \sigma_3(J_2, J_3), \\ &e_1^{e} = e_1^{e}(D_1),\ \ e_2^{e} = e_2^{e}(D_2, D_3),\ \ e_3^{e} = e_3^{e}(D_2, D_3), \end{aligned} \tag{7b}$$

where I_1, J_j and D_k are the stress and strain invariants, '1′ is the "direction" corresponding to the 1st invariant, '2' and '3' are directions forming an orthogonal set to the direction '1' and depend upon the 2nd and 3rd invariants only. We use 1, 2, and 3 to denote the "directions"

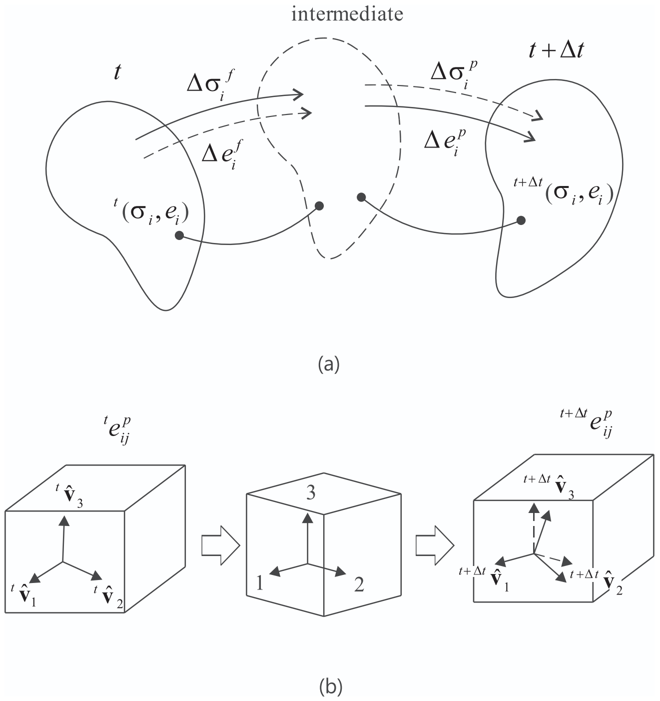

Fig. 3. Solution framework for three-dimensional concrete behaviors. (a) Decomposition of incremental step into phenomena of elastic-fracturing and elasto-plasticity. (b) Evolution of internal state with plastic strain, applied at the intermediate configuration in Fig. 3(a).

and the associated stress and strain quantities, which are identified with the 'compression system' later.

In elasticity, the bulk and shear moduli relate the stresses to the strains as

$$\sigma_J = E_J e_J^e, \tag{7c}$$

$$\begin{gathered} {}^{t}E_1 = K_e,\ {}^{t}E_2 = G_e,\ {}^{t}E_3 = G_e, \\ {}^{t+\Delta t}E_1 = K_s,\ {}^{t+\Delta t}E_2 = G_s,\ {}^{t+\Delta t}E_3 = G_s, \end{gathered} \tag{7d}$$

with ${}^{t}E_J$ (K_e and G_e) and ${}^{t+\Delta t}E_J$ (K_s and G_s) denoting the original and updated (bulk and shear) moduli. The solution of the elasto-plastic-fracturing problem is to solve Eq. (6) where E_e is replaced by ${}^{t}E_J$, E is replaced by ${}^{t+\Delta t}E_J$ with the 3D setting in Eq. (7).

Decomposed solution procedure and coupling between plasticity and fracture

We decompose the solution process to obtain the stress increment using Eq. (7c),

$$\begin{gathered} \Delta\sigma_J = {}^{t+\Delta t}\sigma_J - {}^{t}\sigma_J,\ \Delta E_J = {}^{t+\Delta t}E_J - {}^{t}E_J, \\ \Delta e_J^e = {}^{t+\Delta t}e_J^e - {}^{t}e_J^e, \Delta\sigma_J = \Delta\sigma_J^f + \Delta\sigma_J^p, \end{gathered} \tag{8a}$$

where $\Delta\sigma_J^f$ is the decrease in stress due to fracture with no strain change but a change in the modulus and $\Delta\sigma_J^p$ is the plastic strain increment with no change in modulus

$$\Delta\sigma_J^f = \Delta E_J \cdot e_J^e, \tag{8b}$$

$$\Delta\sigma_J^p = E_J \cdot \Delta e_J^e. \tag{8c}$$

Then we have

$$\begin{gathered} e_J = e_J^e + e_J^p,\ \ \Delta e_J = {}^{t+\Delta t}e_J - {}^{t}e_J = 0, \\ \Delta e_J^e = {}^{t+\Delta t}e_J^e - {}^{t}e_J^e \text{ and } \Delta e_J^p = {}^{t+\Delta t}e_J^p - {}^{t}e_J^p, \\ {}^{t+\Delta t}e_J^p = {}^{t}e_J^p - \Delta e_J^e, \end{gathered} \tag{8d}$$

and the finite element procedures need to establish the change in modulus as well as updating the plastic strain.

It follows from earlier work, see MD Kotsovos and MN Pavlović [31], that the moduli and their changes are given in terms of the current stresses. In fact, the fracture effects in Eq. (8b) can be directly incorporated in the analysis in empirical form by using the new moduli ${}^{t+\Delta t}E_J$ (thus not using ΔE_J and Eqs. (5) and (8b)). We shall use this approach.

The simplified solution process is shown in Fig. 3(a). Fracturing is solved first, and plasticity is solved next: in fracturing we use stress increments directly by substituting the new ${}^{t+\Delta t}E_J$ in Eq. (7d) for Eqs. (8b), (8d), and in plasticity we keep ${}^{t+\Delta t}E_J$ constant and use this constant value to solve the flow equations in Eqs. (8c), (8d). The reason for this order of computations is that fracturing (the change of modulus) is measured elastically, and plastic strain is measured only after the elastic coordinate (Eq. (7)) is set. A different order is possible, resulting in a different accumulation of plastic strains, but our choice is to let plastic strain occur minimally (in the principle of virtual work) with the softened modulus.

When solving for the effects of plasticity, the stresses and strains are

$${}^{t+\Delta t}e_{ij}^{e} = \frac{1}{2G_s}\,{}^{t+\Delta t}\sigma_{ij}^{dev} + \frac{1}{9K_s}\,{}^{t+\Delta t}\sigma_{kk}\delta_{ij}, \tag{9a}$$

$${}^{t+\Delta t}\sigma_{ij} = 2G_s\,{}^{t+\Delta t}e_{ij}^{e,dev} + K_s\,{}^{t+\Delta t}e_{kk}^{e}\delta_{ij}, \tag{9b}$$

and when solving for the effects of fracture, the stresses and strains are

$$\begin{gathered} {}^{t+\Delta t}e_{ij}^{p,dev} = {}^{t+\Delta t}e_{ij}^{p} - \frac{1}{3}\delta_{ij}\,{}^{t+\Delta t}e_{kk}^{p},\ \ {}^{t+\Delta t}e_{ij}^{e} = {}^{t+\Delta t}e_{ij} - {}^{t+\Delta t}e_{ij}^{p}, \\ {}^{t+\Delta t}\sigma_{ij} = 2G_s\,{}^{t+\Delta t}e_{ij}^{e,dev} + \left(K_s\,{}^{t+\Delta t}e_{kk}^{e} - \sigma_{id}\right)\delta_{ij}, \end{gathered} \tag{9c}$$

where plastic strain is present in both steps, see Fig. 3(b). Here σ_{id} is motivated from the volumetric confining effect in the concrete material [31] known as the 'confining pressure', see Ref. [6].

We should note that Eqs. (8) and (9) in essence merge two theories, those published by MD Kotsovos and MN Pavlović [31] and ZP Bažant and SS Kim [6], to account for 'fracturing' and 'plasticity'. The idea of separating the plastic-only calculation from the fracturing-only solution used here is useful for obtaining constitutive law effectively, like it is useful in hierarchical modeling [38].

We briefly presented the basic ingredients of our solution procedure to include fracture and plasticity in the equations given above. In the next two sections, we give some details of how we proceed when considering a multi-dimensional strain and stress state.

2.1.3. *Incorporating fracture*

The changes in the material moduli are based upon the stresses and are empirically given as [31]:

$$\begin{aligned} K_s &= K_e \Big/ \left[1 + A\left(\frac{-\sigma_o}{f_c}\right)^{b-1}\right] \quad \text{if } \frac{-\sigma_o}{f_c} \leqslant 2,\ K_s \\ &= K_e \Big/ \left[1 + 2^{b-1}Ab + 2^{b}(b-1)A\left(\frac{\sigma_o}{f_c}\right)^{-1}\right] \quad \text{if } \frac{-\sigma_o}{f_c} > 2, \end{aligned} \tag{10a}$$

$$G_s = G_e \Big/ \left[1 + c\left(\frac{\tau_o}{f_c}\right)^{d-1}\right],\ \ \sigma_{id} = kf_c\left(\frac{\tau_o}{f_c}\right)^{n} \Big/ \left[1 + l\left(\frac{-\sigma_o}{f_c}\right)^{m}\right], \tag{10b}$$

where σ_o and τ_o are obtained using Eq. (2) for the last converged values of stresses,

and A,b,c,d,k,l,m,n are coefficients that depend upon the cylindrical compressive strength f_c of the concrete material, as discussed in Appendix A. To obtain the constitutive matrix including cracking, also the experimentally measured modulus is used but accounting for the tangential (instantaneous) value instead of the secant value in Eq. (10) [31], that is,

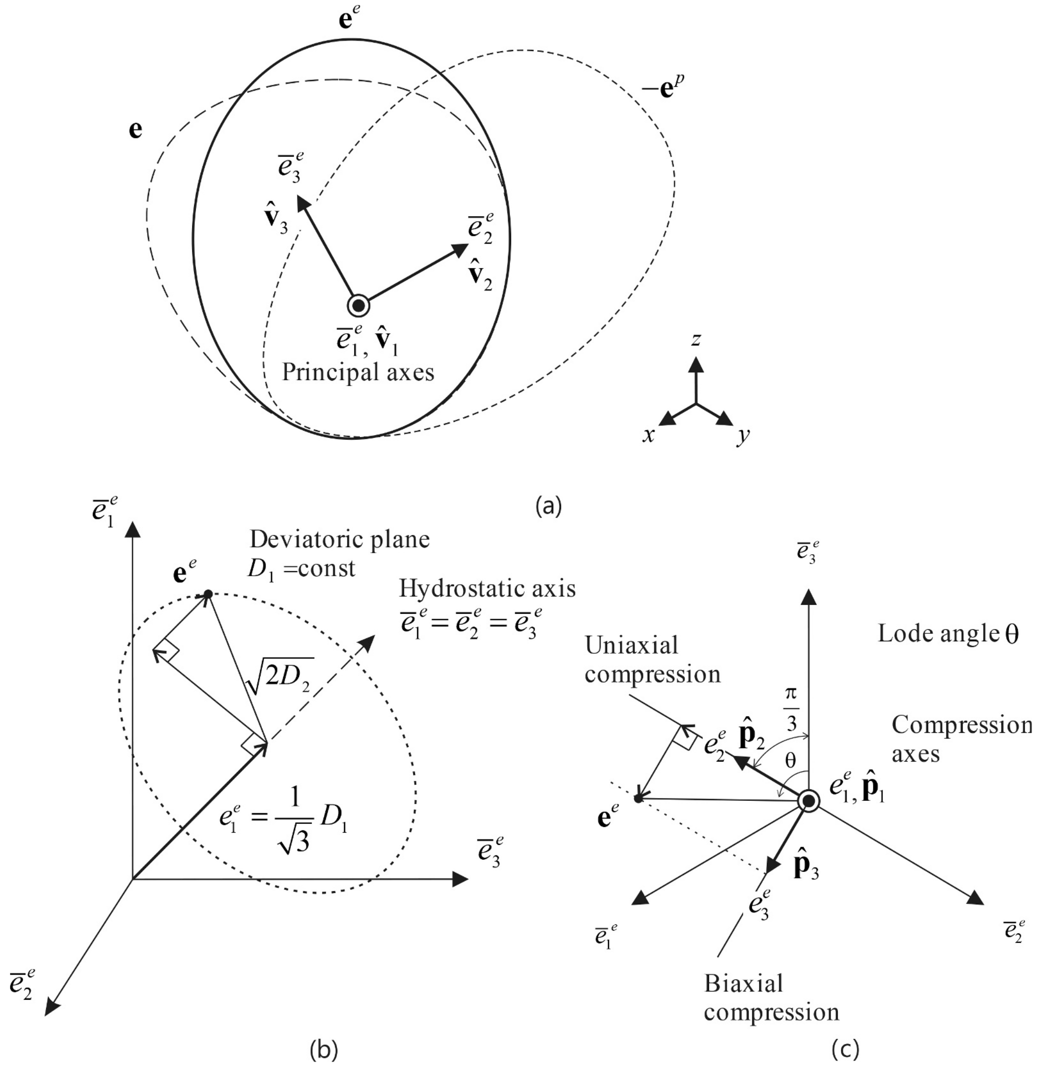

Fig. 4. Coordinate systems of strain definition. (a) Principal coordinate axes ($\overline{e}_1^e$, $\overline{e}_2^e$, $\overline{e}_3^e$) and basis ($\widehat{\boldsymbol{v}}_1$, $\widehat{\boldsymbol{v}}_2$, $\widehat{\boldsymbol{v}}_3$) on elastic strain space. (b) Volumetric-deviatoric separation by hydrostatic axis and deviatoric plane of elastic strain. (c) The compression coordinate axes (e_1^e, e_2^e, e_3^e) and basis ($\widehat{\boldsymbol{p}}_1$, $\widehat{\boldsymbol{p}}_2$, $\widehat{\boldsymbol{p}}_3$) on elastic strain space.

$$
\begin{aligned}
&K_c = K_e \text{ in tension,}\\
&K_c = K_e \Big/ \left[1 + Ab\left(\frac{-\sigma_o}{f_c}\right)^{b-1}\right] \text{ for } \frac{-\sigma_o}{f_c} \leqslant 2 \text{ in compression,}\\
&K_c = \frac{K_e}{1 + 2^{b-1}Ab} \text{ for } \frac{-\sigma_o}{f_c} > 2 \text{ in compression,}
\end{aligned}
\tag{11a}
$$

$$
\begin{aligned}
&G_c = G_e \text{ in tension,}\\
&G_c = G_e \Big/ \left[1 + cd\left(\frac{\tau_o}{f_c}\right)^{d-1}\right] \text{ in compression.}
\end{aligned}
\tag{11b}
$$

These equations are used in the finite element solution. Due to the rational forms of the moduli, using Eq. (7) and differentiating Eqs. (10) and (11), we obtain the empirical form in Eq. (5).

To obtain the updated stress, the increments in the fracture strain and Young's modulus (Δe^f and ΔE) in Eqs. (4c) and (4b) are not used and instead we employ

$$
\Delta\sigma_J^f = -\,{}^{t+\Delta t}E_J \Delta e_J^p,\ \ \Delta e_J^p = -\frac{\Delta\sigma_J^f}{{}^{t+\Delta t}E_J}. \tag{12}
$$

We note that the inelastic effects of Δe^f are expressed in Δe^p, see Fig. 2. Fracture and plasticity are two different phenomena but are coupled through the elastic effects.

2.1.4. Incorporation of plastic flow

We next define two coordinate systems that are key in the development of the finite element procedure. The two coordinate systems are the 'principal system of the elastic strain' and the 'compression system' shown in Fig. 4, which are used simultaneously in the finite element solution procedure.

To describe the plastic flow, we use the coordinate system composed of the current principal directions of the elastic strains

$$
\begin{aligned}
&{}^{t+\Delta t}\boldsymbol{e}^{e(0)} = {}^{t+\Delta t}\boldsymbol{e} - {}^{t+\Delta t}\boldsymbol{e}^{p(0)},\ \ {}^{t+\Delta t}e_{kk}^{e(0)} = {}^{t+\Delta t}e_{kk} - {}^{t+\Delta t}e_{kk}^{p(0)},\\
&{}^{t+\Delta t}e_{ij}^{e,dev(0)} = {}^{t+\Delta t}e_{ij}^{dev} - {}^{t+\Delta t}e_{ij}^{p,dev(0)},\ \text{with } {}^{t+\Delta t}e_{ij}^{p(0)} = {}^{t}e_{ij}^{p},
\end{aligned}
\tag{13a}
$$

$$
\begin{bmatrix}
{}^{t+\Delta t}e_{11}^{e(0)} & {}^{t+\Delta t}e_{12}^{e(0)} & {}^{t+\Delta t}e_{13}^{e(0)}\\
{}^{t+\Delta t}e_{21}^{e(0)} & {}^{t+\Delta t}e_{22}^{e(0)} & {}^{t+\Delta t}e_{23}^{e(0)}\\
{}^{t+\Delta t}e_{31}^{e(0)} & {}^{t+\Delta t}e_{32}^{e(0)} & {}^{t+\Delta t}e_{33}^{e(0)}
\end{bmatrix}
= {}^{t+\Delta t}\boldsymbol{P}
\begin{bmatrix}
{}^{t+\Delta t}\overline{e}_1^{e(0)} & & \\
 & {}^{t+\Delta t}\overline{e}_2^{e(0)} & \\
 & & {}^{t+\Delta t}\overline{e}_3^{e(0)}
\end{bmatrix}
{}^{t+\Delta t}\boldsymbol{P}^T,
\tag{13b}
$$

$$
\begin{aligned}
&{}^{t+\Delta t}\boldsymbol{P} = \left[\ {}^{t+\Delta t}\widehat{\boldsymbol{v}}_1 \quad {}^{t+\Delta t}\widehat{\boldsymbol{v}}_2 \quad {}^{t+\Delta t}\widehat{\boldsymbol{v}}_3\ \right],\ \ \widehat{\boldsymbol{v}}_j\cdot\widehat{\boldsymbol{v}}_k = \delta_{jk},\\
&{}^{t+\Delta t}\overline{e}_1^{e(0)} \geqslant {}^{t+\Delta t}\overline{e}_2^{e(0)} \geqslant {}^{t+\Delta t}\overline{e}_3^{e(0)},\ \ {}^{t+\Delta t}\boldsymbol{P} = {}^{t+\Delta t}\boldsymbol{P}^{(0)} = {}^{t+\Delta t}\boldsymbol{P}^{(N)}.
\end{aligned}
\tag{13c}
$$

$$
\cos 3\theta = \frac{3\sqrt{3}D_3}{2(D_2)^{3/2}}, \tag{13d}
$$

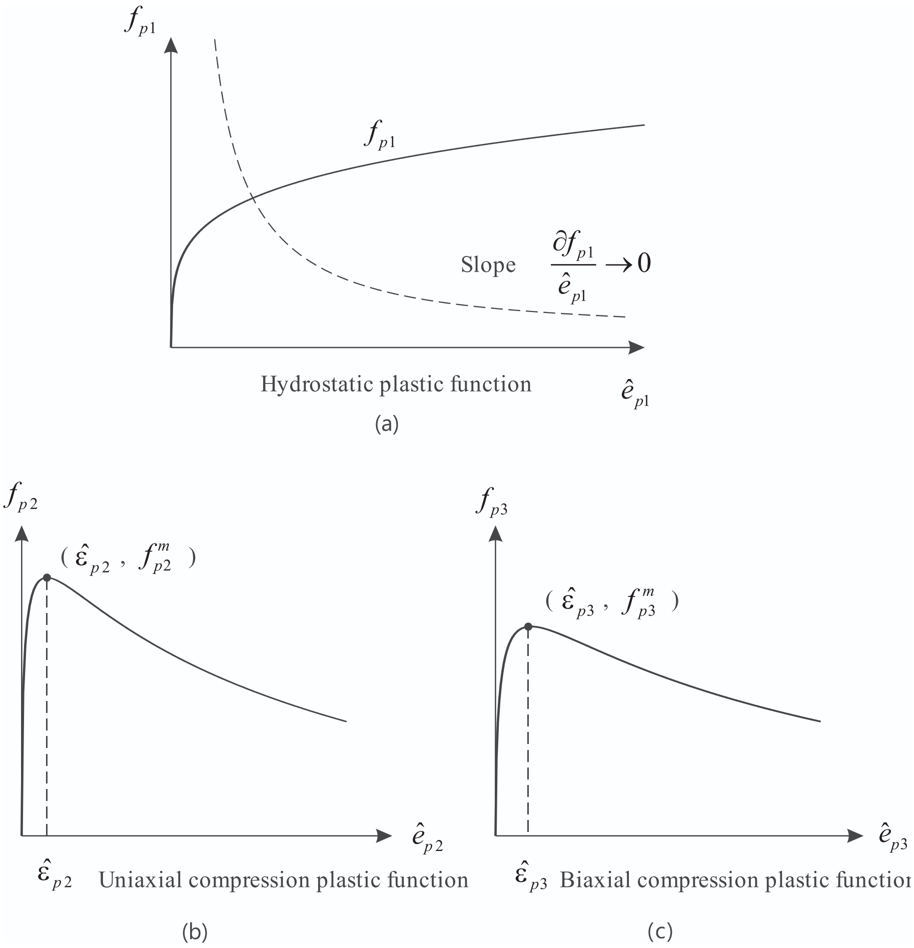

Fig. 5. Plastic functions representing failure surfaces. Plastic curves in (a) hydrostatic compression, (b) uniaxial compression, (c) biaxial compression.

$$\begin{bmatrix} \overline{e}_1^e \\ \overline{e}_2^e \\ \overline{e}_3^e \end{bmatrix} = \frac{D_1}{3}\begin{bmatrix} 1 \\ 1 \\ 1 \end{bmatrix} + \sqrt{\frac{4D_2}{3}}\begin{bmatrix} \cos(\theta) \\ \cos(2\pi/3 - \theta) \\ \cos(2\pi/3 + \theta) \end{bmatrix}, \quad \overline{e}_1^e \geqslant \overline{e}_2^e \geqslant \overline{e}_3^e \ \text{ as } \ 0 \leqslant \theta \leqslant \frac{\pi}{3}. \tag{13e}$$

where ${}^{t+\Delta t}\overline{e}_j^e$ are the principal components ($j = 1..3$) and the $\widehat{\boldsymbol{v}}_j$ form the orthonormal basis corresponding to the principal components. This coordinate system describes the directions of the elastic element deformations, see Fig. 4(a). The strain components in this system are given in Eqs. (7a) and (13d) by the three strain invariants and the Lode angle.

The second system, as introduced in Eqs. (7) and (8c), is the 'compression coordinate system' which is used to obtain the incremental strains ($\Delta \boldsymbol{e}^e$ and $\Delta \boldsymbol{e}^p$) calculated based on the compression of the material. The two systems are used for quite different purposes – to update the elastic strains in the principal elastic strain directions and to calculate the plastic deformations due to the actions of compression. The final results at the end of the step are given in the principal elastic strain coordinate system at $t + \Delta t$.

We will use superscripts '(0)' and '(N)' for the stress and strain quantities in the trial states and at the end of incorporating the effects of plasticity, see Eqs. (8) and (9).

We now use the directions 1, 2, 3 corresponding to the directions of uniaxial compression (e_2^e), biaxial compression (e_3^e) and hydrostatic compression (e_1^e) defined as follows

$$e_1^e = \left| D_1/\sqrt{3} \right|, \ e_2^e = \sqrt{2D_2}\cos(\frac{\pi}{3} - \theta), \ e_3^e = \sqrt{2D_2}\sin(\frac{\pi}{3} - \theta). \tag{14a}$$

$$\begin{aligned} &(\, \overline{e}_1^e \quad \overline{e}_2^e \quad \overline{e}_3^e \,) = e_1^e \widehat{\boldsymbol{p}}_1 + e_2^e \widehat{\boldsymbol{p}}_2 + e_3^e \widehat{\boldsymbol{p}}_3, \\ &\widehat{\boldsymbol{p}}_1 = \left(\frac{1}{\sqrt{3}} \quad \frac{1}{\sqrt{3}} \quad \frac{1}{\sqrt{3}} \right), \ \widehat{\boldsymbol{p}}_2 = \left(\frac{1}{\sqrt{6}} \quad \frac{1}{\sqrt{6}} \quad -\frac{2}{\sqrt{6}} \right), \\ &\widehat{\boldsymbol{p}}_3 = \left(\frac{1}{\sqrt{2}} \quad -\frac{1}{\sqrt{2}} \quad 0 \right), \end{aligned} \tag{14b}$$

$$\begin{aligned} \sqrt{2D_2} &= \sqrt{\left(e_{11}^{e,dev}\right)^2 + \left(e_{22}^{e,dev}\right)^2 + \left(e_{33}^{e,dev}\right)^2 + 2\left(e_{12}^{e,dev}\right)^2 + 2\left(e_{13}^{e,dev}\right)^2 + 2\left(e_{23}^{e,dev}\right)^2} \\ &= \sqrt{\left(e_2^e\right)^2 + \left(e_3^e\right)^2}, \end{aligned} \tag{14c}$$

where the e_j^e ($j = 1..3$) are defined in Eq. (14a) and the three vectors $\widehat{\boldsymbol{p}}$, $\widehat{\boldsymbol{q}}$, $\widehat{\boldsymbol{r}}$ are unit vectors defining the 'compression coordinate system' of quantities in Eq. (7).

For the solution process, we need to relate the components in the principal elastic strain axes to the components in the compression axes of strains, hence Eqs. (13c) and (14c) are used for the transformation. Further verification of the equivalence of Eq. (13e) and Eqs. (14a), (14b) is given in Appendix B.

The plastic strain is decomposed by incremental changes using three separate yield functions corresponding to both the volumetric (first component in compression axes) and the deviatoric (second and third components in compression axes) effects of plastic strain.

The failure surface functions defined in these directions are denoted using the subscript $|(\cdot)$, and the effective strains are defined as $\widehat{e}_j^p$. To extend the plasticity to three individual failure surfaces corresponding to the three compressive directions, we introduce

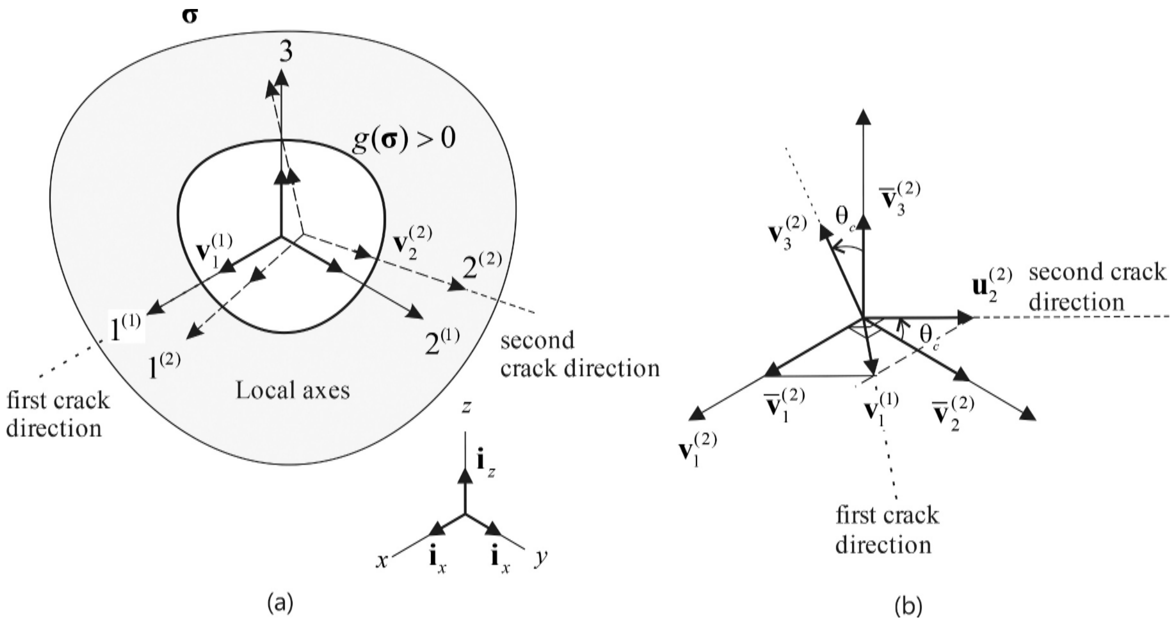

Fig. 6. Quantities used in the evolution of cracks. (a) Local axes for crack directions and crack-failure surfaces. (b) Projection of principal directions to establish the second direction from the first direction.

$$\Delta e_1^p = -\Delta e_1^e,\ \Delta e_2^p = -\Delta e_2^e,\ \Delta e_3^p = -\Delta e_3^e,\\ \Delta e_j^p = \Delta e_{j|1}^p + \Delta e_{j|2}^p + \Delta e_{j|3}^p, \tag{15a}$$

$$\Delta \widehat{e}_j^p = ((\frac{2}{3})\Delta e_j^p \Delta e_j^p)^{1/2}. \tag{15b}$$

The index $j|k$ denotes the strain contribution in direction j corresponding to the failure surface k.

$$f_1 = \left|e_1^e\right| - f_c \cdot f_{p1},\\ f_2 = e_2^e - f_c \cdot f_{p2},\\ f_3 = e_3^e - f_c \cdot f_{p3}. \tag{15c}$$

$$f_{p1} = c_{p1}\left(1+\frac{\widehat{e}_{p1}}{a}\right)^{-s}\widehat{e}_{p1},\\ f_{p2} = c_{p2}\exp[-\left(\frac{\widehat{e}_{p2}}{c_2}\right)^{m_2}]\widehat{e}_{p2},\ f_{p3} = c_{p3}\exp[-\left(\frac{\widehat{e}_{p3}}{c_3}\right)^{m_3}]\widehat{e}_{p3},\\ c_j = (\widehat{\varepsilon}_{pj}) \cdot m_j^{(1/m_j)} \text{ with } j = 2,3 \tag{15d}$$

see Fig. 5. The coefficients used in these relations including the experimental observations in Refs. [9,39–43] are given in Appendix C. However, with the introduction of the strain-solution process, these functions are defined differently from those in the previous literature. The hydrostatic curve is increasing to match the experimental fits in Refs. [39,40,43], with its derivative reaching zero as the plastic strain tends to infinity. Secondly, for uniaxial and biaxial curves, the function decreases with a negative slope and then finally the function and the slope approach 0, but the coefficients c_j are defined differently from those given in Ref. [16], see Appendix C for the detailed derivations and reasons.

To solve for the plastic flow given by $f_j = 0$ ($j = 1..3$) in Eq. (15) we can employ similar schemes as used in standard plasticity [33], but how we utilize the converged material solution to establish the global components (Eqs. (8c) and (13a)) is different due to the introduction of two coordinate systems and three additional characteristics in the flow. The complete update procedure and derivation of the constitutive matrix for the finite element solution are given in Section 2.2.

2.1.5. *Incorporating cracking – Crack opening and closure and tension softening*

For modeling the cracking of the concrete, we apply two approaches in our model: the approach to describe a crack opening and closure with a strength envelope, and also the approach of utilizing smeared crack orientations.

The strength envelope used for crack opening is [31,44]

$$g = \tau_o - \frac{0.944 f_c}{w}\left(t_p - \frac{\sigma_o}{f_c}\right)^{0.724},\ t_p \in [0.05, 0.10],\\ w(e) = \frac{4(1-e^2)cos^2\theta + (2e-1)^2}{2(1-e^2)cos\theta + (2e-1)\sqrt{4(1-e^2)cos^2\theta + 5e^2 - 4e}},\\ e = 0.670551(t_p - \frac{\sigma_o}{f_c})^{0.133}, \tag{16}$$

where t_p is the ratio of the tensile to compressive strengths f_t/f_c, e is the eccentricity of compression to extension on the deviatoric plane ($e = \tau_o|_{\theta=0}/\tau_o|_{\theta=\pi/3}$, see also Fig. 4(b)). We note that $w(e)$ is an elliptic function obtained from the strength envelope in Ref. [44]. Eq. (16) governs material failures after either softening in tension or ductile failure in compression, see Fig. 1.

Considering the possibility of n cracks occurring, $n = 1,2,3$, we apply the smeared crack approach to store the stress orientations as follows

$$\begin{bmatrix} {}^{t+\Delta t}\sigma_{11} & {}^{t+\Delta t}\sigma_{12} & {}^{t+\Delta t}\sigma_{13} \\ {}^{t+\Delta t}\sigma_{21} & {}^{t+\Delta t}\sigma_{22} & {}^{t+\Delta t}\sigma_{23} \\ {}^{t+\Delta t}\sigma_{31} & {}^{t+\Delta t}\sigma_{32} & {}^{t+\Delta t}\sigma_{33} \end{bmatrix} = \overline{\boldsymbol{V}}^{(n)} \begin{bmatrix} {}^{t+\Delta t}\overline{\sigma}_1 & & \\ & {}^{t+\Delta t}\overline{\sigma}_2 & \\ & & {}^{t+\Delta t}\overline{\sigma}_3 \end{bmatrix} \overline{\boldsymbol{V}}^{(n)T}, \tag{17a}$$

$$\overline{\boldsymbol{V}}^{(n)} = [\overline{\boldsymbol{v}}_1^{(n)} \quad \overline{\boldsymbol{v}}_2^{(n)} \quad \overline{\boldsymbol{v}}_3^{(n)}],\ \overline{\boldsymbol{v}}_j^{(n)} \cdot \overline{\boldsymbol{v}}_k^{(n)} = \delta_{jk},\\ {}^{t+\Delta t}\overline{\sigma}_1 \geqslant {}^{t+\Delta t}\overline{\sigma}_2 \geqslant {}^{t+\Delta t}\overline{\sigma}_3,\ n = 1,2,\\ \boldsymbol{V}^{(n)} = [\boldsymbol{v}_1^{(n)} \quad \boldsymbol{v}_2^{(n)} \quad \boldsymbol{v}_3^{(n)}],\ \boldsymbol{V}^{(3)} = \boldsymbol{V}^{(2)};\ \boldsymbol{v}_j^{(1)} = \overline{\boldsymbol{v}}_j^{(1)}\ j = 1,3,\ \boldsymbol{v}_1^{(2)} = \overline{\boldsymbol{v}}_1^{(2)},\\ \boldsymbol{v}_2^{(2)} = \cos(\theta_c)\overline{\boldsymbol{v}}_2^{(2)} + \sin(\theta_c)\overline{\boldsymbol{v}}_3^{(2)},\ \boldsymbol{v}_3^{(2)} = -\sin(\theta_c)\overline{\boldsymbol{v}}_2^{(2)} + \cos(\theta_c)\overline{\boldsymbol{v}}_3^{(2)}, \tag{17b}$$

Table 1
Overview of concrete material solution process.

	For solution steps:
	Current time $= t + \Delta t$, previous time $=t$, material solution iteration counter $k = (0), \ldots I, I+1, \cdots, (N)$; crack solution counter $m = (0), \ldots, (1)$
1. Trial elastic -fracture (Predictor stage)	**Known quantities are** ${}^{t}\boldsymbol{\sigma},\ {}^{t}\boldsymbol{e},\ {}^{t}\boldsymbol{e}^{p},\ {}^{t+\Delta t}\boldsymbol{e}$, for strain evolution $\tau_o^{\max},\ {}^{t}\sigma_o,\ {}^{t}\tau_o$, for solution classification **Calculate** trial strain ${}^{t+\Delta t}\boldsymbol{e}^{e(0)} = {}^{t+\Delta t}\boldsymbol{e} - {}^{t}\boldsymbol{e}^{p}$ (Eq.(13)), **Use new moduli due to fracture (See Section 2.1.3)** Obtain $K_s,\ G_s,\ \sigma_{id}$ with ${}^{t}\sigma_o,\ {}^{t}\tau_o$. (Eq.(10)) ${}^{t+\Delta t}\sigma_{ij}^{(0)} = 2G_s\,{}^{t+\Delta t}e_{ij}^{e,dev(0)} + \left(K_s\,{}^{t+\Delta t}e_{kk}^{e(0)} - \sigma_{id}\right)\delta_{ij}$, (Eq. (9c)) update current state ${}^{t+\Delta t}\sigma_o,\ {}^{t+\Delta t}\tau_o$. (Eq. (2)) In case there is no compressive loading go to 2–1, if otherwise go to 2–2.
2-1. Solution without flow (${}^{t+\Delta t}\sigma_o \geqslant 0$ or ${}^{t+\Delta t}\tau_o \leqslant \tau_o^{\max}$)	**Calculate** stresses (see Section 2.1.2) ${}^{t+\Delta t}\sigma_{ij}^{(N)} = {}^{t}\sigma_{ij}^{(N)} + C_{ijkl}^{E}\left({}^{t+\Delta t}e_{ij}^{e(0)} - {}^{t}e_{ij}^{e(0)}\right)$(Eq.(26))and update the internal state, straight from (0) to (N) in this solution step ${}^{t+\Delta t}e_{ij}^{e(N)} = \frac{1}{2G_s}\,{}^{t+\Delta t}\sigma_{ij}^{dev(N)} + \frac{1}{9K_s}\,{}^{t+\Delta t}\sigma_{kk}^{(N)}\delta_{ij}$(Eq.(9a)) ${}^{t+\Delta t}e_{ij}^{p} = {}^{t}e_{ij}^{p} - {}^{t+\Delta t}e_{ij}^{e(N)} + {}^{t+\Delta t}e_{ij}^{e(0)}$. The constitutive law is now C_{ijkl}^{E} **End of solution to include effects of fracture**
2–2. Flow in Compressive loading (${}^{t+\Delta t}\sigma_o < 0$ and ${}^{t+\Delta t}\tau_o > \tau_o^{\max}$)	**Apply plastic flow solution (See Section 2.1.4)** **Initialize** the directions ${}^{t+\Delta t}\boldsymbol{P}$ and Lode angle θ with ${}^{t+\Delta t}\boldsymbol{e}^{e(0)}$. (Eq.(13)) **Evaluate** ${}^{t+\Delta t}e_1^{e(0)} = \lvert D_1\rvert/\sqrt{3},\ {}^{t+\Delta t}e_2^{e(0)} = \sqrt{2D_2}\cos(\frac{\pi}{3} - \theta)$, ${}^{t+\Delta t}e_3^{e(0)} = \sqrt{2D_2}\sin(\frac{\pi}{3} - \theta),\ D_1,\ D_2$ with ${}^{t+\Delta t}\boldsymbol{e}^{e(0)}$(Eq. (14a)) **Iterate** ${}^{t+\Delta t}\lambda_j^{(I+1)} = {}^{t+\Delta t}\lambda_j^{(I)} + \Delta\lambda_j,\ {}^{t+\Delta t}e_j^{e(I+1)} = {}^{t+\Delta t}e_j^{e(I)} - \Delta e_j^{p}$, ${}^{t+\Delta t}e_j^{p(I+1)} = {}^{t+\Delta t}e_j^{p(I)} + \Delta e_j^{p}$, (Eq. (29c)) and solve until $\lVert f_i^{(N)}\rVert <$ Tol, where Tol is the convergence tolerance used. **After convergence calculate** $(D_1)' = \sqrt{3}\,{}^{t+\Delta t}e_1^{e(N)},\ \sqrt{2(D_2)'} = {}^{t+\Delta t}e_2^{e(N)}\cos(\frac{\pi}{3} - \theta) +$ ${}^{t+\Delta t}e_3^{e(N)}\sin(\frac{\pi}{3} - \theta),\ \begin{bmatrix} {}^{t+\Delta t}\overline{e}_1^{e(N)} \\ {}^{t+\Delta t}\overline{e}_2^{e(N)} \\ {}^{t+\Delta t}\overline{e}_3^{e(N)} \end{bmatrix} = \frac{(D_1)'}{3}\begin{bmatrix} 1 \\ 1 \\ 1 \end{bmatrix} sgn(D_1) +$ $\sqrt{\frac{4(D_2)'}{3}}\begin{bmatrix} \cos(\theta) \\ \cos(\frac{2\pi}{3} - \theta) \\ \cos(\frac{2\pi}{3} + \theta) \end{bmatrix}$, (Eq.(30)) Evaluate the strains and stresses using the solution (N) in Eq. (9b) ${}^{t+\Delta t}\sigma_{ij}^{(N)} = 2G_s\,{}^{t+\Delta t}e_{ij}^{e,dev(N)} + K_s\,{}^{t+\Delta t}e_{kk}^{e(N)}\delta_{ij}$.(Eq. (9b)) Calculate $\boldsymbol{C} = \boldsymbol{C}^{E} - \boldsymbol{C}^{P}$ with K_s, G_s, corresponding to $\lambda_i^{(N)}$, establish the tangent values $\frac{\partial g_i}{\partial e_k^e},\ \widehat{e}_i^{p(N)} =$ $\left((\frac{2}{3})\frac{\partial g_i^{(N)}}{\partial e_k^e}\frac{\partial g_i^{(N)}}{\partial e_k^e}\right)^{1/2}\lambda_i^{(N)}$. (Eq. (27c)) **End of plastic-fracturing solution**
3. Cracking (compression or tension) ($n = {}^{t+\Delta t}\boldsymbol{n}^{(m)}$; 0 for closure, $n = 1, 2, 3$ for cracks,$>$3 for crushing)	**Trial Stage (Crack opening)** If $g({}^{t+\Delta t}\sigma_{ij}^{(N)}) > 0$ (${}^{t+\Delta t}\sigma_o < 0$ or ${}^{t+\Delta t}\sigma_o \geqslant 0$) then ${}^{t+\Delta t}\boldsymbol{n}^{(0)} = {}^{t}\boldsymbol{n} + 1$. Crushing occurs for ${}^{t+\Delta t}\boldsymbol{n}^{(0)} > 3$ and all stresses and the constitutive law are set to zero. Obtain $\boldsymbol{V}^{(n)}$, $\boldsymbol{T}^{(n)T}$ and $\boldsymbol{W}^{(n)}$. Calculate ${}^{t+\Delta t}\overline{\boldsymbol{e}}^{C} = \boldsymbol{T}^{(n)T}\,{}^{t+\Delta t}\boldsymbol{e}^{e}$, determine crack closure. (Eq.(18a)). **Crack solution** If the crack is open, ${}^{t+\Delta t}\boldsymbol{n}^{(1)} = {}^{t+\Delta t}\boldsymbol{n}^{(0)}$, calculate stresses with ${}^{t+\Delta t}\boldsymbol{\sigma} = {}^{t}\boldsymbol{\sigma} + \boldsymbol{C}^{C(n)}\left({}^{t+\Delta t}\boldsymbol{e}^{e} - {}^{t}\boldsymbol{e}^{e}\right)$ or ${}^{t+\Delta t}\boldsymbol{\sigma} = \boldsymbol{T}^{(n)}\,{}^{t+\Delta t}\overline{\boldsymbol{\sigma}}^{C(n)} + \boldsymbol{C}^{C(n)}\left({}^{t+\Delta t}\boldsymbol{e}^{e} - {}^{t}\boldsymbol{e}^{e}\right)$ and ${}^{t+\Delta t}\overline{\boldsymbol{\sigma}}^{C(n)} =$ $\boldsymbol{W}^{(n)}\ {}^{t}\boldsymbol{\sigma}$,apply tension-softening. If the crack is closed, solution progresses with reduced number of crack, or if ${}^{t+\Delta t}n = 0$, go to calculations in 2.1 or 2.2 for the non-cracked state

$$\begin{aligned}
&\tan\theta_c = -\frac{\overline{\boldsymbol{v}}_1^{(1)}\cdot\overline{\boldsymbol{v}}_2^{(2)}}{\overline{\boldsymbol{v}}_1^{(1)}\cdot\overline{\boldsymbol{v}}_3^{(2)}},\ \boldsymbol{v}_j^{(n)} = v_{jx_k}^{(n)}\boldsymbol{i}_{x_k},\ x_1 = x,\ x_2 = y,\ x_3 = z,\\
&\boldsymbol{T}^{(n)} = [T_{IJ}^{(n)}] = [T_{ijkl}^{(n)}],\ \boldsymbol{W}^{(n)} = [W_{IJ}^{(n)}] = [W_{ijkl}^{(n)}],\ I = ij,\ J = kl,\\
&T_{ijkl}^{(n)} = \frac{1}{2}\left(v_{kx_i}^{(n)}v_{lx_j}^{(n)} + v_{lx_i}^{(n)}v_{kx_j}^{(n)}\right)\ \text{ for } k = l,\\
&T_{ijkl}^{(n)} = \left(v_{kx_i}^{(n)}v_{lx_j}^{(n)} + v_{lx_i}^{(n)}v_{kx_j}^{(n)}\right)\ \text{ for } k \neq l,\\
&W_{ijkl}^{(n)} = \frac{1}{2}\left(v_{ix_k}^{(n)}v_{jx_l}^{(n)} + v_{ix_l}^{(n)}v_{jx_k}^{(n)}\right)\ \text{ for } k = l,\\
&W_{ijkl}^{(n)} = \left(v_{ix_k}^{(n)}v_{jx_l}^{(n)} + v_{ix_l}^{(n)}v_{jx_k}^{(n)}\right)\ \text{ for } k \neq l,
\end{aligned}\tag{17c}$$

The $\overline{\boldsymbol{V}}^{(n)}$ give the local orientation of a new crack, the superscript (n) denotes the nth crack, $\boldsymbol{V}^{(n)}$ is the rotated orientation for the crack, $\boldsymbol{T}$ and $\boldsymbol{W}$ are the transformation matrices from the local to the global and the global to the local Cartesian systems, respectively, $\boldsymbol{i}_{x_k}$ are the 'global axes' for the global Cartesian coordinates, see Fig. 6. When $g({}^{t+\Delta t}\sigma_{ij}) > 0$, cracking occurs in the direction $\boldsymbol{v}_n^{(n)}$ of the largest principal stress for the (n)th new crack. In later cracks, with a larger value of (n), the directions are aligned to be orthogonal to any crack already formed.

In case the attempt is that $(n) > 3$, see Table 1, crushing occurs resulting in zero stress, a constitutive law with all zero entries, and no further history is measured at that material point.

Given the crack orientations, we update the current crack status accounting for the previous history. With the crack strain $\overline{e}_n^{C(n)}$ available $(n = 1, 2, 3)$, the crack closure condition is given by

$${}^{t+\Delta t}\overline{\boldsymbol{e}}^{C(n)} = \boldsymbol{T}^{(n)T}\ {}^{t+\Delta t}\boldsymbol{e}^{e},\ \overline{\boldsymbol{e}}^{C(n)} = [\overline{e}_I^{C(n)}] = [\overline{e}_{ij}^{C(n)}],\tag{18a}$$

$$0 < {}^{t+\Delta t}\overline{e}_n^{C(n)} \leqslant \max_{\tau=0..t}\left({}^{\tau}\overline{e}_n^{C(n)}\right).\tag{18b}$$

A finite element can contain up to three new cracks at a location, and if an orientation in Eq. (17) is the same as previously obtained ($\boldsymbol{V}^{(n)} = \boldsymbol{V}^{(n-1)}$ with $n \geqslant 2$) or the tensile crack strain does not exceed the previous maximum strain as defined in Eq. (18b), the number of cracks is reduced to $(n - 1)$.

With the number of cracks ${}^{t+\Delta t}n$ determined for the $t + \Delta t$ state, the following corresponding stresses and constitutive matrices for the cracked state are used (here $n = {}^{t+\Delta t}n$)

$${}^{t+\Delta t}\overline{\boldsymbol{\sigma}}^{C(n)} = \boldsymbol{W}^{(n)}\ {}^{t}\boldsymbol{\sigma},\ \overline{\boldsymbol{\sigma}}^{C(n)} = [\overline{\sigma}_I^{C(n)}] = [\overline{\sigma}_{ij}^{C(n)}],\tag{19a}$$

additionally

$$\begin{aligned}
&{}^{t+\Delta t}\overline{\sigma}_{11}^{C(1)} = 0\ \text{ if } n = 1,\ {}^{t+\Delta t}\overline{\sigma}_{11}^{C(2)} = {}^{t+\Delta t}\overline{\sigma}_{33}^{C(2)} = 0\ \text{ if } n = 2,\\
&\quad {}^{t+\Delta t}\overline{\sigma}_{11}^{C(3)} = {}^{t+\Delta t}\overline{\sigma}_{22}^{C(3)} = {}^{t+\Delta t}\overline{\sigma}_{33}^{C(3)} = 0\ \text{ if } n = 3,
\end{aligned}\tag{19b}$$

$${}^{t+\Delta t}\boldsymbol{\sigma} = {}^{t}\boldsymbol{\sigma} + \boldsymbol{C}^{C(n)}\left({}^{t+\Delta t}\boldsymbol{e}^{e} - {}^{t}\boldsymbol{e}^{e}\right)\ \text{ if } {}^{t+\Delta t}n \leqslant {}^{t}n,\tag{20a}$$

$$\begin{aligned}
&{}^{t+\Delta t}\boldsymbol{\sigma} = \boldsymbol{T}^{(n)}\,{}^{t+\Delta t}\overline{\boldsymbol{\sigma}}^{C(n)} + \boldsymbol{C}^{C(n)}\left({}^{t+\Delta t}\boldsymbol{e}^{e} - {}^{t}\boldsymbol{e}^{e}\right)\\
&\quad \text{with }\ \boldsymbol{C}^{C(n)} = \boldsymbol{T}^{(n)}\overline{\boldsymbol{C}}^{C}\boldsymbol{T}^{(n)T}\ \text{ if } {}^{t+\Delta t}n > {}^{t}n,
\end{aligned}\tag{20b}$$

with $\boldsymbol{C}^{C(n)} = [C_{IJ}^{C(n)}] = [C_{ijkl}^{C(n)}]$,
$\overline{\boldsymbol{C}}^{C(n)} = [\overline{C}_{IJ}^{C(n)}] = [\overline{C}_{ijkl}^{C(n)}]$ with nonzero components for respective the n

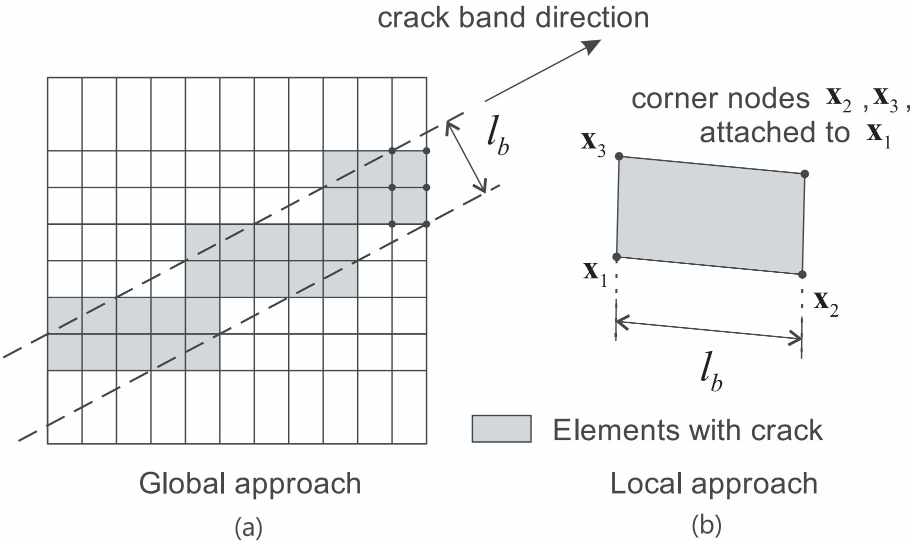

Fig. 7. Determination of the length scale. (a) Global approach, as the effective width of the crack band. (b) Local approach, as the element length.

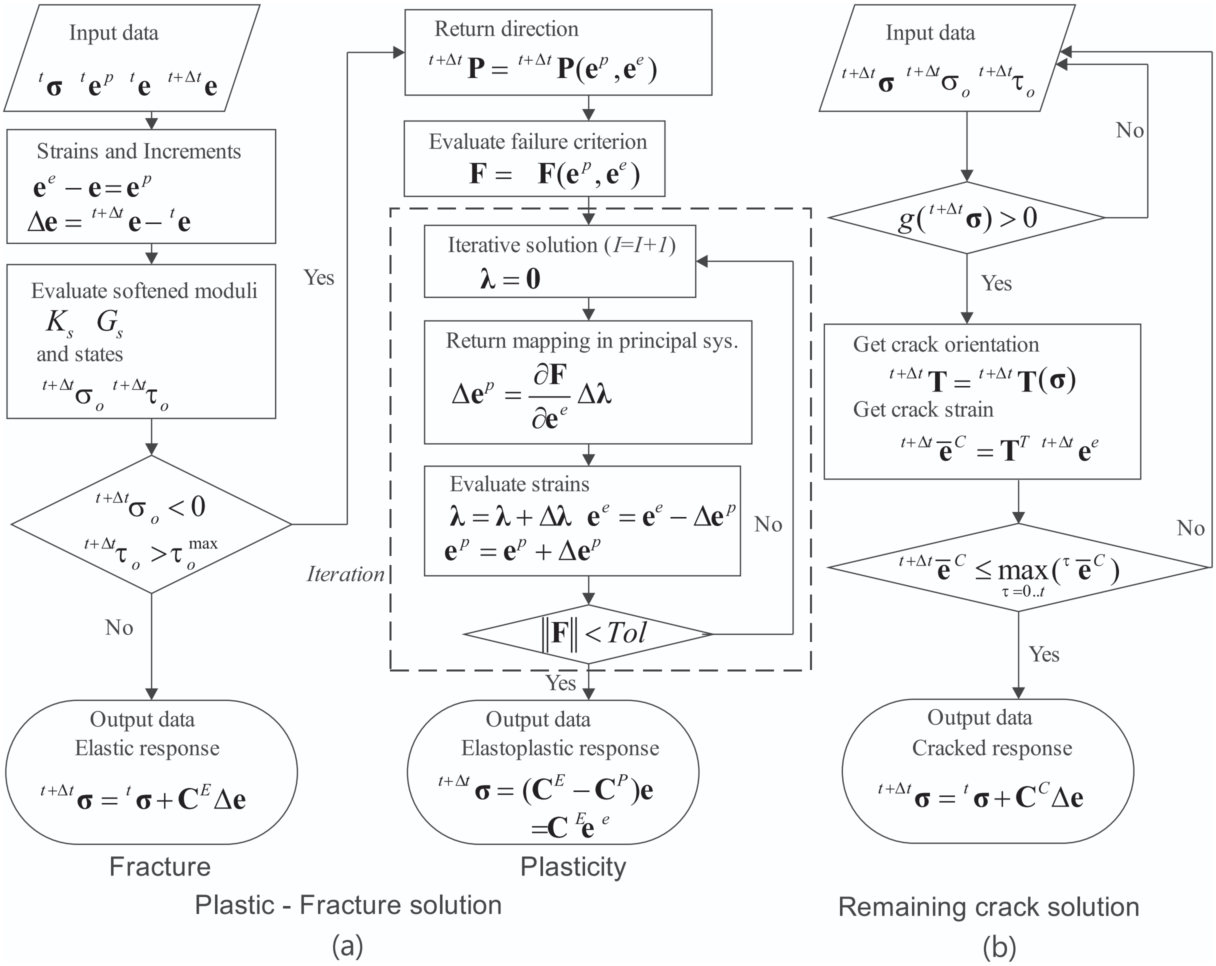

Fig. 8. Flow chart of the solution process. (a) Fracture and plasticity coupled solution. (b) Crack solution. Scalar operations are applied to each component of the vector.

Table 2
Input parameters for the material model.

	Parameters
Parametersalways given(range)	f_c compressive strength ($f_c > 0$) t_p ratio of tensile to compressive strength ($5\%\leqslant t_p\leqslant 10\%$) G_F fracture energy ($G_F\geqslant 0$) per unit area
Optional parameters(overwriting the built-in parameters)	E Young's modulus for initial strength ν Poisson's ratio for initial strength l_b length scale for fracture energy

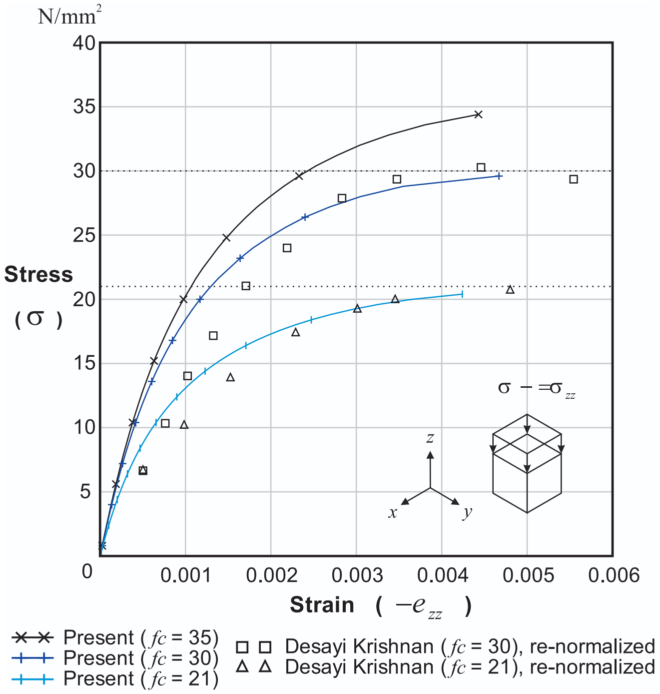

Fig. 9. Stress–strain responses in the uniaxial compression test.

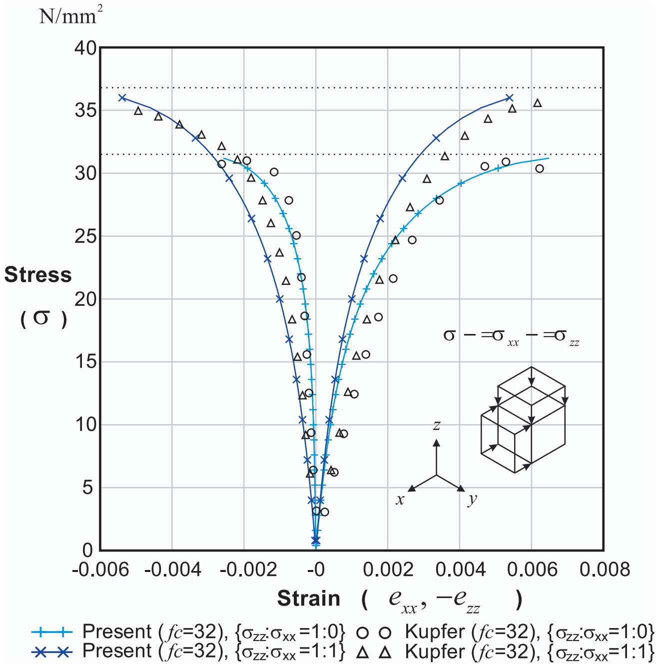

Fig. 10. Stress–strain responses in the biaxial compression test.

$$\overline{C}^{C(1)}_{1111} = \eta^N\lambda_a,\ \overline{C}^{C(1)}_{2222} = \overline{C}^{C(1)}_{3333} = \lambda_a,\ \overline{C}^{C(1)}_{2233} = \overline{C}^{C(1)}_{3322} = \lambda_c,$$
$$\overline{C}^{C(1)}_{1212} = \overline{C}^{C(1)}_{1313} = \eta^S G_c,\ \overline{C}^{C(1)}_{2323} = G_c \quad \text{if } n = 1;$$
$$\overline{C}^{C(2)}_{1111} = \overline{C}^{C(2)}_{3333} = \eta^N\lambda_a,\ \overline{C}^{C(2)}_{2222} = \lambda_a,\ \overline{C}^{C(2)}_{1212} = \overline{C}^{C(2)}_{1313} = \overline{C}^{C(2)}_{2323} = \eta^S G_c \quad \text{if } n = 2;$$
$$\overline{C}^{C(3)}_{1111} = \overline{C}^{C(3)}_{2222} = \overline{C}^{C(3)}_{3333} = \eta^N\lambda_a,\ \overline{C}^{C(3)}_{1212} = \overline{C}^{C(3)}_{1313} = \overline{C}^{C(3)}_{2323} = \eta^S G_c \quad \text{if } n = 3;$$
$$\lambda_c = K_c - \frac{2}{3}G_c,\ \lambda_a = \lambda_c + 2G_c,\ \eta^N = 0.0001,\ \eta^S = 0.1, \tag{21}$$

with similar entries given in Ref. [1] for a fixed crack.

Lastly, to use the fracture energy G_F and tensile crack strain $\overline{e}^{C(n)}_n$, Eqs. (19b), (21) are modified as

$$\text{if } \overline{\varepsilon}^{TP}\leqslant\overline{e}^{C(n)}_n\leqslant\overline{\varepsilon}^{TU} \quad \text{with} \quad \overline{\varepsilon}^{TU} = \frac{2G_F}{f_c\cdot t_p\cdot l_b},\ \overline{\varepsilon}^{TP} = \frac{f_c\cdot t_p}{K_e + \frac{4}{3}G_e},$$
$$G_F = \frac{1}{2}(f_c\cdot t_p)(\overline{\varepsilon}^{TU}\cdot l_b) \quad \text{with length scale } l_b, \tag{22}$$

$$\overline{C}^{C(1)}_{11} = \overline{C}^{TS},\ {}^{t+\Delta t}\overline{\sigma}^{C(1)}_{11} = {}^{t+\Delta t}\overline{\sigma}^{TS} \quad \text{if } n = 1;$$
$$\overline{C}^{C(2)}_{11} = \overline{C}^{C(2)}_{33} = \overline{C}^{TS},\ {}^{t+\Delta t}\overline{\sigma}^{C(2)}_{11} = {}^{t+\Delta t}\overline{\sigma}^{C(2)}_{33} = {}^{t+\Delta t}\overline{\sigma}^{TS} \quad \text{if } n = 2;$$
$$\overline{C}^{TS} = \frac{-f_c\cdot t_p}{(\overline{\varepsilon}^{TP} - \overline{\varepsilon}^{TU})},\ {}^{t+\Delta t}\overline{\sigma}^{TS} = \frac{f_c\cdot t_p}{(\overline{\varepsilon}^{TP} - \overline{\varepsilon}^{TU})}(\overline{\varepsilon}^{TU} - {}^{t+\Delta t}\overline{e}^{C(n)}_n), \tag{23}$$

which is known as a tension-softening effect where the brittle behavior is changed into ductile behavior, see Fig. 1. The 'length scale' l_b which normalizes tensile strain $\overline{\varepsilon}^{TU}$ for crack closure as well as the fracture energy can be given either locally or globally in two different ways. Firstly, it can be given as a material input parameter, applied globally as the effective width of the crack band formed by elements containing the cracks, see Fig. 7(a), by adopting the approach in M Jirásek and M Bauer [45]. Secondly, when it is not specified ($l_b = 0$ from global input), it can be locally given as the maximum side length of the element on which the material quantities are evaluated, $l_b = \max(\|\boldsymbol{x}_1 - \boldsymbol{x}_2\|, \|\boldsymbol{x}_1 - \boldsymbol{x}_3\|, \|\boldsymbol{x}_1 - \boldsymbol{x}_4\|)$ where $\boldsymbol{x}_2$, $\boldsymbol{x}_3$, $\boldsymbol{x}_4$ are coordinates of the nodes attached to a corner node at $\boldsymbol{x}_1$, see Fig. 7(b). The two methods respectively correspond to the 'non-local' or 'local' interpretation of crack, see [22].

2.1.6. *Incorporating reinforcement*

We can use two approaches for incorporating reinforcement: In the first approach, 1D truss elements are attached compatibly to solid elements in the mesh in the physical directions of the reinforcement. In the second approach, the smeared reinforcement approach, the elements possessing fictitious thickness $\rho_r \times t$ are additionally attached to the solid elements, where ρ_r is referred as the 'reinforcement ratio' for the concrete thickness t. See Section 3 for examples of modeling the reinforcement in these ways.

The approaches described in this section are applicable in 2D and 3D finite element solutions. In the case of plane stress conditions, the components normal to the plane are statically condensed out.

2.2. *The complete solution process*

As described in detail in Ref. [34], the geometric and material nonlinearities can be described using the Total Lagrangian formulation given by the governing principle of virtual work

$${}^{t+\Delta t}R = \int_{{}^0V} {}^{t+\Delta t}_{\ \ 0}S_{ij}\,\delta\,{}^{t+\Delta t}_{\ \ 0}\varepsilon_{ij}\,d\,{}^0V, \tag{24a}$$

where ${}^{t+\Delta t}R$ is the external virtual work, ${}^{t+\Delta t}_{\ \ 0}S_{ij}$ and ${}^{t+\Delta t}_{\ \ 0}\varepsilon_{ij}$ are the 2nd Piola-Kirchhoff stress and Green-Lagrange strain tensors, respectively, and ${}^0V$ is the domain considered in the reference configuration. The linearization of the governing principle of virtual work about the

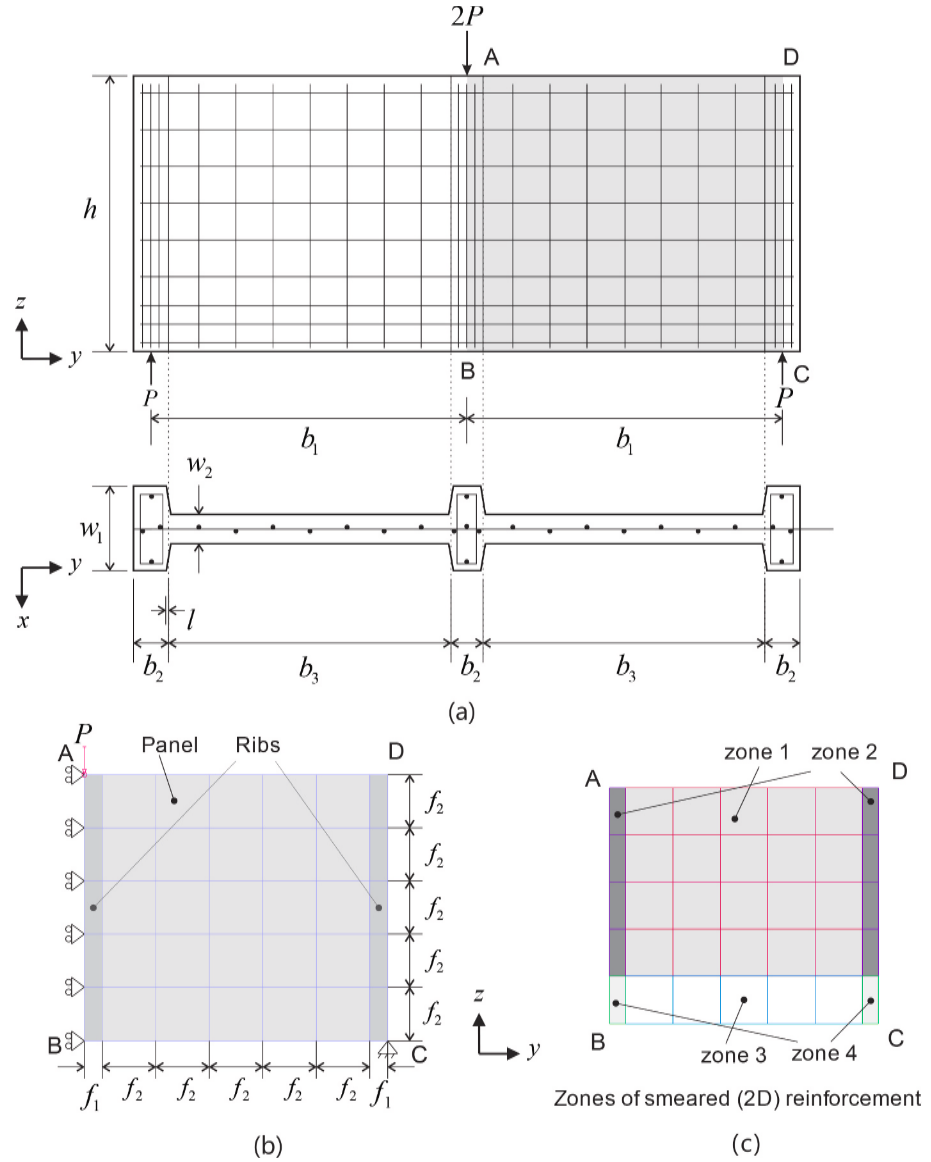

Fig. 11. The concrete panel (W-2) problem. (a) Problem definition ($h = 762\,\text{mm}, w_1 = 298.5\,\text{mm}, w_2 = 76.2\,\text{mm}, l = 0.95\,\text{mm}, b_1 = 864\,\text{mm}, b_2 = 101.6\,\text{mm}, b_3 = 762\,\text{mm}$). (b) Finite element idealization ($f_1 = 51\,\text{mm}, f_2 = 152\,\text{mm}, f_3 = 154\,\text{mm}$). (c) Zones of smeared reinforcement. Further details are given in Table 4 in [mm, N, MPa].

Table 3
Input parameters for the panel.

Parameters from the present model
f_c, t_p (0.05), $G_F, l_b = 0.0$

configuration at time t gives [34]

$$\int_{{}^0V} {}_0C_{ijrs}\, {}_0e_{rs}\delta\, {}_0e_{ij} d\,{}^0V + \int_{{}^0V} {}^t_0S_{ij}\delta\, {}_0\eta_{ij} d\,{}^0V = {}^{t+\Delta t}R - \int_{{}^0V} {}^t_0S_{ij}\delta\, {}_0e_{ij} d\,{}^0V, \tag{24b}$$

where ${}_0e_{ij}$ and ${}_0\eta_{ij}$ are the linear and nonlinear parts of the Green-Lagrange strain tensor, respectively, and ${}_0C_{ijrs}$ is the tangent stress–-strain relation. Eq. (24) is a general relation for small and large strains and large rotations. However, when modeling concrete, we can assume small-strain conditions, which nevertheless may also contain large displacements and rotations. Hence, to develop the solution procedure, we can focus on the material-nonlinear-only case of Eq. (24), and use [34]

$$\int_V C_{ijrs} e_{rs} \delta e_{ij} dV = {}^{t+\Delta t}R - \int_V {}^t\sigma_{ij} \delta e_{ij} dV, \tag{25a}$$

with

$$d\sigma_{ij} = C_{ijrs} de_{rs}, \quad {}^{t+\Delta t}\sigma_{ij} = {}^t\sigma_{ij} + d\sigma_{ij}, \tag{25b}$$

where ${}^{t+\Delta t}\sigma_{ij}$ is the Cauchy stress, e_{ij} is the infinitesimally small strain, C_{ijrs} is the constitutive law relating the incremental stress to the total incremental strain, and all quantities are measured in the 'global coordinate system' for the finite element analysis.

We should note, however, that although we focus on the material-nonlinear-only case of Eq. (24), merely to give the solution steps, we need to use the Total Lagrangian formulation of Eq. (24) if we want to include large displacement/ large rotation effects (with the small strain assumption). The material law used in that case is the same as used in Eq. (25), see Ref. [34].

An overview of the complete solution process is given in Table 1. The strain update from the solution of elastic-fracturing or elasto-plasticity is

Table 4
Modeling details (Concrete and reinforcement properties) of the panel considered.

	Zones			
	Zone 1 (top panel)	Zone 2 (top ribs)	Zone 3 (bottom panel)	Zone 4 (bottom ribs)
Concrete properties f_c	$f_c = 26.8$			
Reinforcement properties f_{yy}, f_{zz}, E_{yy}, E_{zz}.	Yield strength in $y-$ and $z-$ directions $f_{yy} = f_{zz} = 353$, Orthotropic Young's moduli in $y-$ and $z-$ directions $E_{yy} = E_{zz} = 190000$, respectively, and the corresponding tangent moduli $E^T_{yy} = 0$, $E^T_{zz} = 0$.			
Thickness	$t^{s1} = w_2$	$t^{s2} = w_1$	$t^{s3} = w_2$	$t^{s4} = w_1$
Reinforce ratio in y-direction	$\rho^{s1}_{yy} = 0.0092$	$\rho^{s2}_{yy} = 0.0023$	$\rho^{s3}_{yy} = 0.0183$	$\rho^{s4}_{yy} = 0.0047$
Smeared thickness for y-direction	$\rho^{s1}_{yy} t^{s1} = 0.7010$	$\rho^{s2}_{yy} t^{s2} = 0.6866$	$\rho^{s3}_{yy} t^{s3} = 1.394$	$\rho^{s4}_{yy} t^{s4} = 1.403$
Reinforce ratio in z-direction	$\rho^{s1}_{zz} = 0.0092$	$\rho^{s2}_{zz} = 0.0047$	$\rho^{s3}_{zz} = 0.0092$	$\rho^{s4}_{zz} = 0.0047$
Smeared thickness for z-direction	$\rho^{s1}_{zz} t^{s1} = 0.7010$	$\rho^{s2}_{zz} t^{s2} = 1.403$	$\rho^{s3}_{zz} t^{s3} = 0.7010$	$\rho^{s4}_{zz} t^{s4} = 1.403$

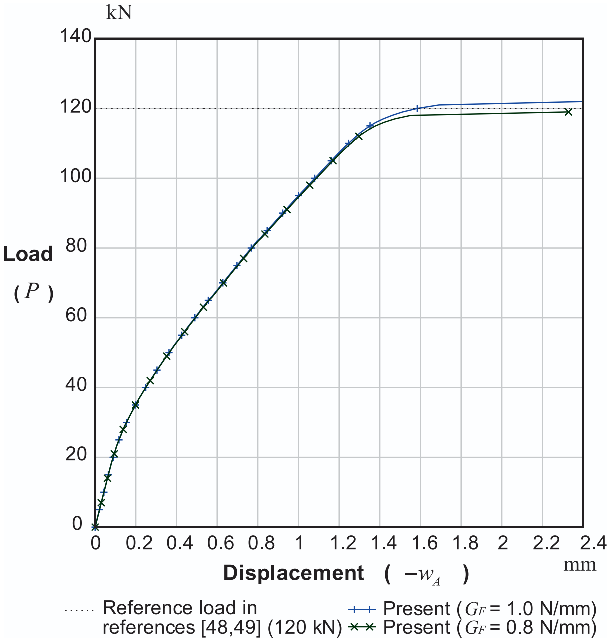

Fig. 12. Calculated load–displacement curves.

denoted using the material counter $k = (0), \cdots, I, I+1, \ldots, (N)$ and the history of a new crack is denoted using m to account for a change in crack status.

In case we have tensile behavior, or the material is in a state of unloading (given by ${}^{t+\Delta t}\tau_o < \tau_o^{\max}$ in Eq. (2)), we solve for the incremental linear solution of the stress as in Ref. [1], but for the material state we obtain the new strain using Eq. (9b), and update the internal 'inelastic strain' using Eq. (8d).

$$
\begin{aligned}
&{}^{t+\Delta t}\sigma^{(N)}_{ij} = {}^{t}\sigma^{(N)}_{ij} + C^E_{ijkl}({}^{t+\Delta t}e^{e(0)}_{ij} - {}^{t}e^{e(0)}_{ij}), \quad {}^{t}e^{e(0)}_{ij} = {}^{t}e_{ij} - {}^{t-\Delta t}e^{p}_{ij}, \\
&C^E_{ijkl} = (K - \frac{2}{3}G)\delta_{ij}\delta_{kl} + 2G\cdot\frac{1}{2}(\delta_{ik}\delta_{jl} + \delta_{il}\delta_{jk}), \\
&K = K_e, \; G = G_e \; \text{ if tensile state}, \\
&K = K_s, \; G = G_s \; \text{ if unloading in compression},
\end{aligned} \tag{26a}
$$

$$
\begin{aligned}
{}^{t+\Delta t}e^{e(N)}_{ij} &= \frac{1}{2G_s}\,{}^{t+\Delta t}\sigma^{dev(N)}_{ij} + \frac{1}{9K_s}\,{}^{t+\Delta t}\sigma^{(N)}_{kk}\delta_{ij}, \quad {}^{t+\Delta t}e^{p}_{ij} \\
&= {}^{t}e^{p}_{ij} - {}^{t+\Delta t}e^{e(N)}_{ij} + {}^{t+\Delta t}e^{e(0)}_{ij}.
\end{aligned} \tag{26b}
$$

where *(N)* denotes the final state of the updated stress. Update of plastic strain in Eq. (26b) comes from coupling of plasticity and fracture in elastic medium as introduced in Eqs. (8), (9) with intermediate configuration in Fig. 3. The constitutive law in Eq. (25b) is $C_{ijkl} = C^E_{ijkl}$ in this tensile or unloading state. If cracking occurs, the constitutive law reflects it using $C_{ijkl} = C^{C(n)}_{ijkl}$ in Eq. (20). See Table 1 for details.

In loading under compression, the total flow is updated with the associated flow rule as follows:

$$
\begin{aligned}
&\lambda^{(0)}_1 = 0, \; \lambda^{(0)}_2 = 0, \; \lambda^{(0)}_3 = 0, \\
&\Delta e^p_{j|1} = \frac{\partial g_1}{\partial e^e_j}\Delta\lambda_1, \; \Delta e^p_{j|2} = \frac{\partial g_2}{\partial e^e_j}\Delta\lambda_2, \; \Delta e^p_{j|3} = \frac{\partial g_3}{\partial e^e_j}\Delta\lambda_3, \\
&g_i = f_i,
\end{aligned} \tag{27a}
$$

where we note that the total plastic strain increment (in direction j) is a result of all contributions from the three failure surfaces in the compression coordinate system:

$$
\Delta e^p_j = \sum_{k=1}^{3} \Delta e^p_{j|k} = \Delta e^p_{j|1} + \Delta e^p_{j|2} + \Delta e^p_{j|3}. \tag{27b}
$$

$$
\Delta \widehat{e}^p_i = ((\frac{2}{3})\frac{\partial g_i}{\partial e^e_k}\frac{\partial g_i}{\partial e^e_k})^{1/2}\Delta\lambda_i = \Lambda_i \Delta\lambda_i, \; \text{ with } \Lambda_i = ((\frac{2}{3})\frac{\partial g_i}{\partial \mathbf{e}^e} : \frac{\partial g_i}{\partial \mathbf{e}^e})^{1/2}, \tag{27c}
$$

and the yield function is linearized as

$$
f^{(I+1)}_i = f^{(I)}_i + (\frac{\partial f^{(I)}_i}{\partial e^e_j})\Delta e^e_j + \sum_{j=1}^{3}\frac{\partial f^{(I)}_i}{\partial \widehat{e}^p_j}\Delta \widehat{e}^p_j = 0. \tag{27d}
$$

With this new incremental equation composed of strains-only (with yield function f_i and potential function g_i) we derive a process updating the global stresses and the constitutive law.

Combining Eqs. (8d), (27a), (27b), and using Eqs. (15), (27c) we obtain the terms in Eq. (27d),

$$
\begin{aligned}
(\frac{\partial f^{(I)}_i}{\partial e^e_j})\Delta e^e_j &= (\frac{\partial f^{(I)}_i}{\partial e^e_j})(-\Delta e^p_{j|1} - \Delta e^p_{j|2} - \Delta e^p_{j|3}), \\
&= -(\frac{\partial f^{(I)}_i}{\partial e^e_j})\frac{\partial g^{(I)}_1}{\partial e^e_j}\Delta\lambda_1 - (\frac{\partial f^{(I)}_i}{\partial e^e_j})\frac{\partial g^{(I)}_2}{\partial e^e_j}\Delta\lambda_2 - (\frac{\partial f^{(I)}_i}{\partial e^e_j})\frac{\partial g^{(I)}_3}{\partial e^e_j}\Delta\lambda_3,
\end{aligned} \tag{28a}
$$

$$
\begin{aligned}
&\frac{\partial f^{(I)}_i}{\partial \widehat{e}^p_j} = \frac{\partial f^{(I)}_i}{\partial \widehat{e}^p_i}\delta_{ij} = -(c_{pi}f_c)\cdot\frac{\partial f^{(I)}_{pi}}{\partial \widehat{e}^p_i}\delta_{ij}, \\
&\frac{\partial f^{(I)}_i}{\partial \widehat{e}^p_j}\Delta\widehat{e}^p_j = -(c_{pi}f_c)\frac{\partial f^{(I)}_{pi}}{\partial \widehat{e}^p_i}\delta_{ij}\cdot((\frac{2}{3})\frac{\partial g^{(I)}_i}{\partial e^e_k}\frac{\partial g^{(I)}_i}{\partial e^e_k})^{1/2}\Delta\lambda_i.
\end{aligned} \tag{28b}
$$

Substituting Eq. (28) into Eq. (27d), we obtain

$$
\begin{aligned}
&(\frac{\partial f^{(I)}_i}{\partial e^e_k})\frac{\partial g^{(I)}_1}{\partial e^e_k}\Delta\lambda_1 + (\frac{\partial f^{(I)}_i}{\partial e^e_k})\frac{\partial g^{(I)}_2}{\partial e^e_k}\Delta\lambda_2 + (\frac{\partial f^{(I)}_i}{\partial e^e_k})\frac{\partial g^{(I)}_3}{\partial e^e_k}\Delta\lambda_3 \\
&+ (c_{p1}f_c)\cdot((\frac{2}{3})\frac{\partial g^{(I)}_1}{\partial e^e_k}\frac{\partial g^{(I)}_1}{\partial e^e_k})^{1/2}\Delta\lambda_1 + (c_{p2}f_c)\cdot((\frac{2}{3})\frac{\partial g^{(I)}_2}{\partial e^e_k}\frac{\partial g^{(I)}_2}{\partial e^e_k})^{1/2}\Delta\lambda_2 \\
&+ (c_{p3}f_c)\cdot((\frac{2}{3})\frac{\partial g^{(I)}_3}{\partial e^e_k}\frac{\partial g^{(I)}_3}{\partial e^e_k})^{1/2}\Delta\lambda_3 = f^{(I)}_i,
\end{aligned} \tag{29a}
$$

$$
\begin{aligned}
&\boldsymbol{A}^{(I)}\Delta\boldsymbol{\lambda} = \boldsymbol{F}^{(I)}, \; \Delta\boldsymbol{\lambda} = [\,\Delta\lambda_1 \quad \Delta\lambda_2 \quad \Delta\lambda_3\,]^T, \; \boldsymbol{F}^{(I)} = [\,f^{(I)}_1 \quad f^{(I)}_2 \quad f^{(I)}_3\,]^T, \\
&\boldsymbol{A}^{(I)} = [A^{(I)}_{ij}] = [\frac{\partial f^{(I)}_i}{\partial e^e_k}\frac{\partial g^{(I)}_j}{\partial e^e_k}] + [(c_{pi}f_c)\frac{\partial f^{(I)}_{pi}}{\partial \widehat{e}^p_i}\delta_{ij}\cdot\Lambda_i],
\end{aligned} \tag{29b}
$$

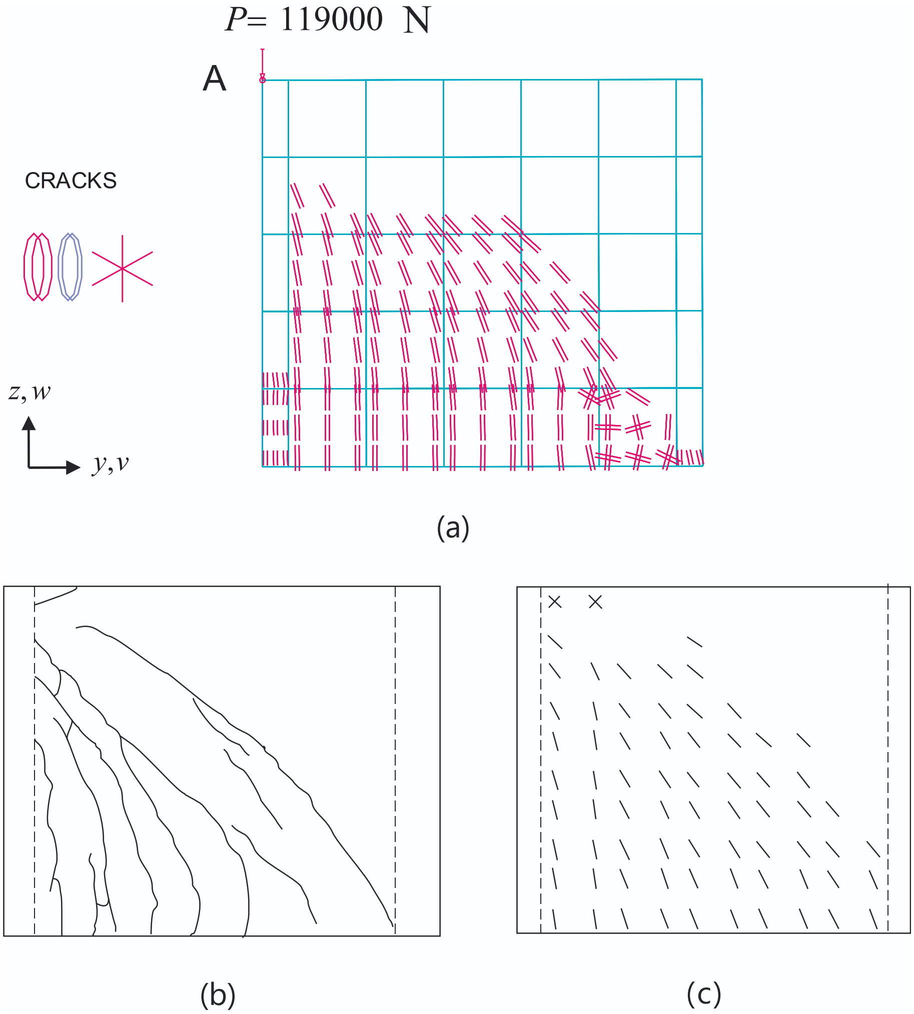

Fig. 13. Cracking at limit state of panel. (a) Predicted response with our concrete model. (b) Experimental result obtained by V Cervenka and KH Gerstle [48]. (c) Numerical result given in HG Kwak and DY Kim [50].

along with the updates to the strains and the total magnitude of flow

$$
{}^{t+\Delta t}\lambda_j^{(I+1)} = {}^{t+\Delta t}\lambda_j^{(I)} + \Delta\lambda_j, \quad {}^{t+\Delta t}e_j^{e(I+1)} = {}^{t+\Delta t}e_j^{e(I)} - \Delta e_j^p, \quad {}^{t+\Delta t}e_j^{p(I+1)} = {}^{t+\Delta t}e_j^{p(I)} + \Delta e_j^p. \tag{29c}
$$

Once convergence has been reached using Eqs. (9), (13), (14), the stresses and strains in the global coordinate system are obtained by applying the inverse transformations

$$
\begin{aligned}
&(D_1)' = \sqrt{3}\,{}^{t+\Delta t}e_1^{e(N)}, \\
&\sqrt{2(D_2)'} = {}^{t+\Delta t}e_2^{e(N)}\cos\left(\frac{\pi}{3}-\theta\right) + {}^{t+\Delta t}e_3^{e(N)}\sin\left(\frac{\pi}{3}-\theta\right),
\end{aligned} \tag{30a}
$$

$$
\begin{aligned}
&\begin{bmatrix} {}^{t+\Delta t}\overline{e}_1^{e(N)} \\ {}^{t+\Delta t}\overline{e}_2^{e(N)} \\ {}^{t+\Delta t}\overline{e}_3^{e(N)} \end{bmatrix} = \frac{(D_1)'}{3}\begin{bmatrix} 1 \\ 1 \\ 1 \end{bmatrix} sgn(D_1) + \sqrt{\frac{4(D_2)'}{3}}\begin{bmatrix} \cos(\theta) \\ \cos\left(\frac{2\pi}{3}-\theta\right) \\ \cos\left(\frac{2\pi}{3}+\theta\right) \end{bmatrix}, \\
&{}^{t+\Delta t}\overline{e}_1^{e(N)} \geqslant {}^{t+\Delta t}\overline{e}_2^{e(N)} \geqslant {}^{t+\Delta t}\overline{e}_3^{e(N)},
\end{aligned} \tag{30b}
$$

$$
\begin{aligned}
&\begin{bmatrix} {}^{t+\Delta t}e_{11}^{e(N)} & {}^{t+\Delta t}e_{12}^{e(N)} & {}^{t+\Delta t}e_{13}^{e(N)} \\ {}^{t+\Delta t}e_{21}^{e(N)} & {}^{t+\Delta t}e_{22}^{e(N)} & {}^{t+\Delta t}e_{23}^{e(N)} \\ {}^{t+\Delta t}e_{31}^{e(N)} & {}^{t+\Delta t}e_{32}^{e(N)} & {}^{t+\Delta t}e_{33}^{e(N)} \end{bmatrix} \\
&= {}^{t+\Delta t}\boldsymbol{P}\begin{bmatrix} {}^{t+\Delta t}\overline{e}_1^{e(N)} & & \\ & {}^{t+\Delta t}\overline{e}_2^{e(N)} & \\ & & {}^{t+\Delta t}\overline{e}_3^{e(N)} \end{bmatrix}{}^{t+\Delta t}\boldsymbol{P}^T,
\end{aligned} \tag{30c}
$$

$$
\begin{aligned}
&{}^{t+\Delta t}\sigma_{ij}^{(N)} = 2G_s\,{}^{t+\Delta t}e_{ij}^{e,dev(N)} + K_s\,{}^{t+\Delta t}e_{kk}^{e(N)}\delta_{ij}, \\
&{}^{t+\Delta t}e_{ij}^{e,dev(N)} = {}^{t+\Delta t}e_{ij}^{e(N)} - \frac{1}{3}\delta_{ij}\,{}^{t+\Delta t}e_{kk}^{e(N)}.
\end{aligned} \tag{30d}
$$

The constitutive matrix is given in the compression coordinate system using Eqs. (7) and (14),

$$
\boldsymbol{G} = [G_{IJ}] = \left[\frac{\partial(\sigma_I)}{\partial(e_J^e)}\right] = \begin{bmatrix} K_s & & \\ & G_s & \\ & & G_s \end{bmatrix}, \tag{31a}
$$

$$
\widehat{e}_i^{p(N)} = \Lambda_i^{(N)}\lambda_i^{(N)}, \quad \boldsymbol{M} = \left[\,\widehat{e}_1^{p(N)} \quad \widehat{e}_2^{p(N)} \quad \widehat{e}_3^{p(N)}\,\right]^T, \tag{31b}
$$

$$
\boldsymbol{C}^{ph} = \left[C_{IJ}^{ph}\right] = \left[\frac{\partial(\sigma_I)}{\partial(e_J)}\right] = \frac{(\boldsymbol{GM})(\boldsymbol{GM})^T}{\boldsymbol{M}^T\boldsymbol{GM}}, \tag{31c}
$$

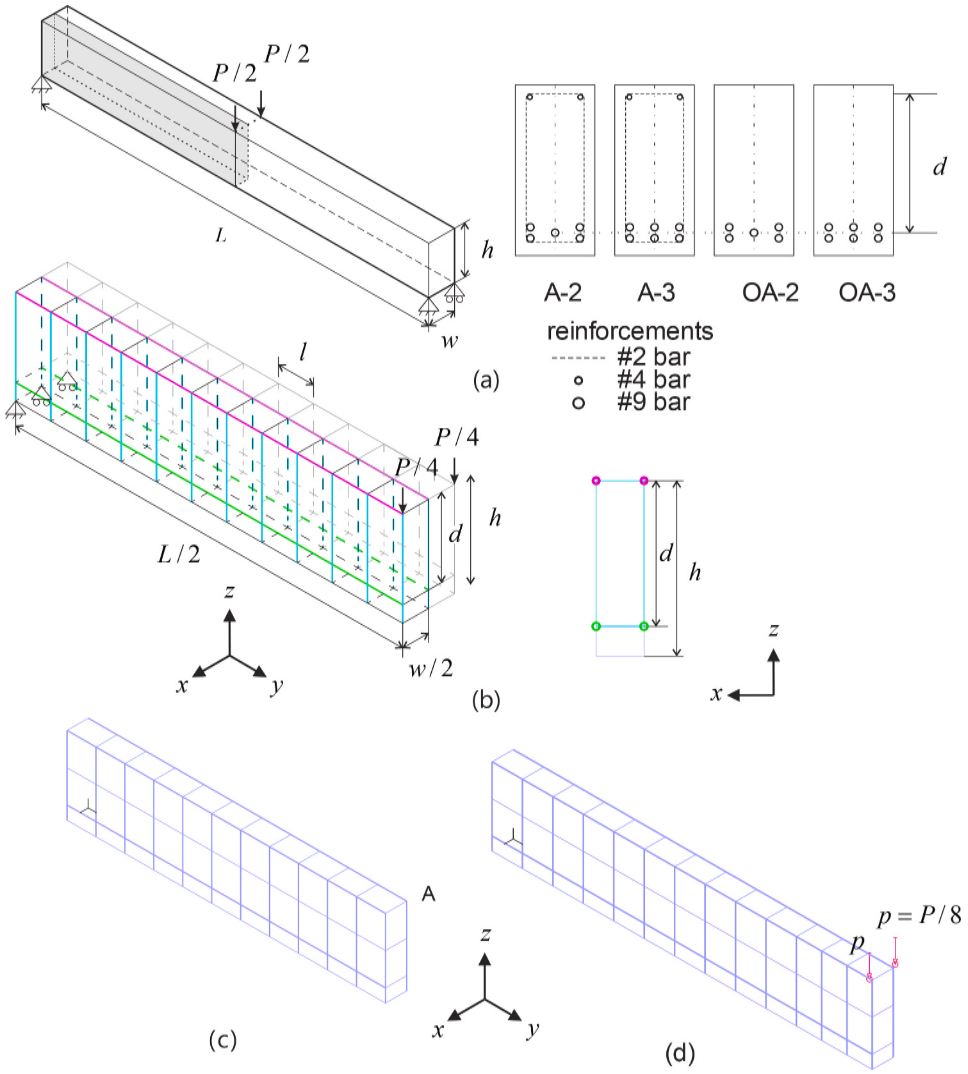

Fig. 14. Scordelis-Bresler series of reinforced-concrete beams. (a) Problem definition with section profiles and reinforcements. (b) Modeling idealization. (c) Mesh used for A-2 and OA-2 beams (d) Mesh used for A-3 and OA-3 beams. Beam height h, depth d and length L; total center load P. For the OA-2 and OA-3 beams only bottom horizontal (#9) bar stiffeners are used, for the A-2 and A-3 beams, all stiffeners (bottom horizontal (#9) bars, top horizontal (#4) bars and vertical (#2) bars are used. The vertical stiffeners are spaced using $l = 210$ mm. Further dimensions and properties are given in Tables 6 and 7 in [mm, N, MPa].

where the plastic contribution to the constitutive matrix in the compression coordinate system is used as a subtraction from the elastic constitutive matrix [33]

$$
\begin{aligned}
&L_J = \frac{1}{\sqrt{3}}\frac{\partial(\sigma_1)}{\partial(e_J)}\cdot sgn(I_1^e),\ N_J = \frac{\partial(\sigma_2)}{\partial(e_J)}\cos(\frac{\pi}{3}-\theta) + \frac{\partial(\sigma_3)}{\partial(e_J)}\sin(\frac{\pi}{3}-\theta),\\
&\frac{\partial(\overline{\sigma}_1)}{\partial(e_J)} = L_J + \sqrt{\frac{2}{3}}N_J\cos(\theta),\ \frac{\partial(\overline{\sigma}_2)}{\partial(e_J)} = L_J + \sqrt{\frac{2}{3}}N_J\cos(\frac{2\pi}{3}-\theta),\\
&\frac{\partial(\overline{\sigma}_3)}{\partial(e_J)} = L_J + \sqrt{\frac{2}{3}}N_J\cos(\frac{2\pi}{3}+\theta),\\
&K_I = \frac{1}{\sqrt{3}}\frac{\partial(\overline{\sigma}_I)}{\partial(e_1)}\cdot sgn(I_1^e),\ S_I = \frac{\partial(\overline{\sigma}_I)}{\partial(e_2)}\cos(\frac{\pi}{3}-\theta) + \frac{\partial(\overline{\sigma}_I)}{\partial(e_3)}\sin(\frac{\pi}{3}-\theta),\\
&\frac{\partial(\overline{\sigma}_I)}{\partial(\overline{e}_J)} = K_I + \sqrt{\frac{2}{3}}S_I\cos(\theta),\ \frac{\partial(\overline{\sigma}_2)}{\partial(\overline{e}_J)} = K_I + \sqrt{\frac{2}{3}}S_I\cos(\frac{2\pi}{3}-\theta),\\
&\frac{\partial(\overline{\sigma}_3)}{\partial(\overline{e}_J)} = K_I + \sqrt{\frac{2}{3}}S_I\cos(\frac{2\pi}{3}+\theta), \boldsymbol{C}^{pr} = [C_{IJ}^{pr}] = [\frac{\partial(\overline{\sigma}_I)}{\partial(\overline{e}_J)}],
\end{aligned}
\tag{31d}
$$

Table 5
Input parameters for the beam.

Parameters from the present model
f_c, t_p (0.10), G_F (0.46 N/mm); $l_b = 0.0$ or specified

$$
\begin{aligned}
&\boldsymbol{C} = \boldsymbol{C}^E - \boldsymbol{C}^P,\ \boldsymbol{C} = [C_{ijkl}],\ \boldsymbol{C}^E = [C_{ijkl}^E],\ \boldsymbol{C}^P = [C_{ijkl}^P] = [\frac{\partial(\sigma_{ij})}{\partial(e_{kl})}],\\
&T_{lJ}^1 = \widehat{v}_{1x_l}\frac{\partial(\overline{\sigma}_1)}{\partial(\overline{e}_J)},\ T_{lJ}^2 = \widehat{v}_{2x_l}\frac{\partial(\overline{\sigma}_2)}{\partial(\overline{e}_J)},\ T_{lJ}^3 = \widehat{v}_{3x_l}\frac{\partial(\overline{\sigma}_3)}{\partial(\overline{e}_J)},\\
&O_{ij}^{1m} = \widehat{v}_{1x_m}\frac{\partial(\sigma_{ij})}{\partial(\overline{e}_J)},\ O_{ij}^{2m} = \widehat{v}_{2x_m}\frac{\partial(\sigma_{ij})}{\partial(\overline{e}_J)},\ O_{ij}^{3m} = \widehat{v}_{3x_m}\frac{\partial(\sigma_{ij})}{\partial(\overline{e}_J)},\\
&\frac{\partial(\sigma_{ij})}{\partial(\overline{e}_J)} = \widehat{v}_{1x_j}T_{iJ}^1 + \widehat{v}_{2x_j}T_{iJ}^2 + \widehat{v}_{3x_j}T_{iJ}^3,\ \frac{\partial(\sigma_{ij})}{\partial(e_{kl})} = \widehat{v}_{1x_l}O_{ij}^{1k} + \widehat{v}_{2x_l}O_{ij}^{2k} + \widehat{v}_{3x_l}O_{ij}^{3k},
\end{aligned}
\tag{31e}
$$

with $\widehat{\boldsymbol{v}}_i = \widehat{v}_{ix_i}\boldsymbol{i}_{x_i}$ in Eq. (13), C_{ijkl}^E is given from Eq. (26) with $K = K_s,\ G = G_s$.

We should note that the material solution process in Eq. (31) and the

Table 6
Modeling details (Geometry and concrete properties) of Scordelis-Bresler beams.

	Beam types			
	OA-2	OA-3	A-2	A-3
Concrete properties f_c	$f_c = 23.7$	$f_c = 37.6$	$f_c = 24.3$	$f_c = 35.1$
Section geometries b,h	$b = 305$, $h = 561$	$b = 305$, $h = 561$	$b = 305$, $h = 561$	$b = 305$, $h = 561$
Effective depth d(idealized location of bar #9), effective section area A	$d = 466$, $A = b{\cdot}d$	$d = 466$, $A = b{\cdot}d$	$d = 466$, $A = b{\cdot}d$	$d = 466$, $A = b{\cdot}d$
Half effective length $L/2$	$L/2 = 2286$	$L/2 = 2743$	$L/2 = 2286$	$L/2 = 2743$
Bottom reinforcement. Total section area of reinforcement A_s	5 #9 bars $A_s = 3226$	6 #9 bars $A_s = 3894$	5 #9 bars $A_s = 3226$	6 #9 bars $A_s = 3894$
Top reinforcement	–	–	2 #4 bars	2 #4 bars
Vertical shear reinforcements	#2 bars, spacing l	#2 bars, spacing l	#2 bars, spacing l	#2 bars, spacing l
Reinforcement ratio of bottom bars	$\rho_r = A_s/A = 0.0227$	$\rho_r = A_s/A = 0.0274$	$\rho_r = A_s/A = 0.0227$	$\rho_r = A_s/A = 0.0274$

Table 7
Modeling details (reinforcement properties) of Scordelis-Bresler beams.

	Reinforcement types			
	#2 bar	#4 bar	#9 bar	#9 bar
area	32.258	125.81	658.06	658.06
Young's modulus E tangent modulus E_T	189.60×10^3 1.8960×10^3	201.32×10^3 2.0132×10^3	217.87×10^3 2.1787×10^3	217.87×10^3 2.1787×10^3
Yield strength f_y	$f_y = 325.43$	$f_y = 345.43$	$f_y = 555.028$	$f_y = 555.27$
remark	–	–	For 2-seriesOA-2,A-2 only	For 3-seriesOA-3,A-3 only

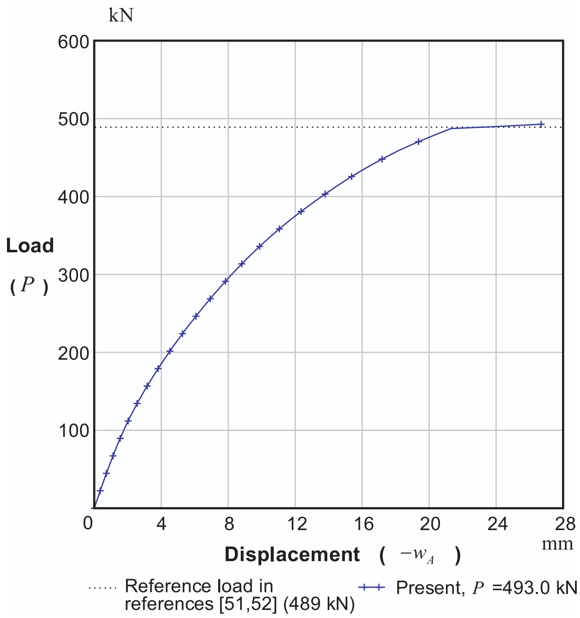

Fig. 15. Load-displacement curve of the A-2 beam.

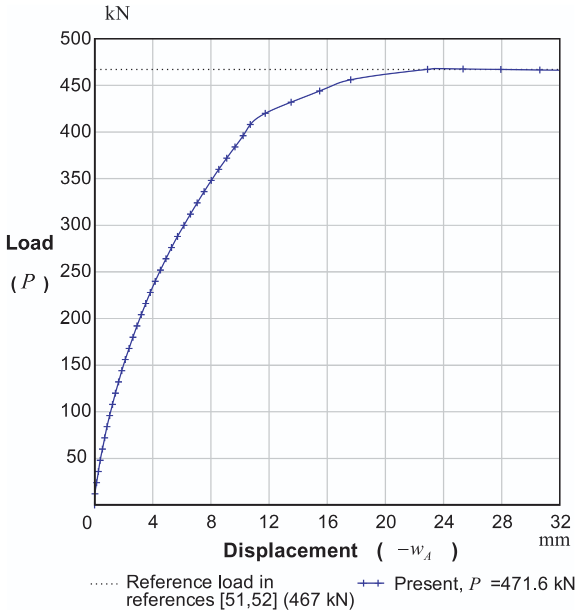

Fig. 16. Load-displacement curve of the A-3 beam.

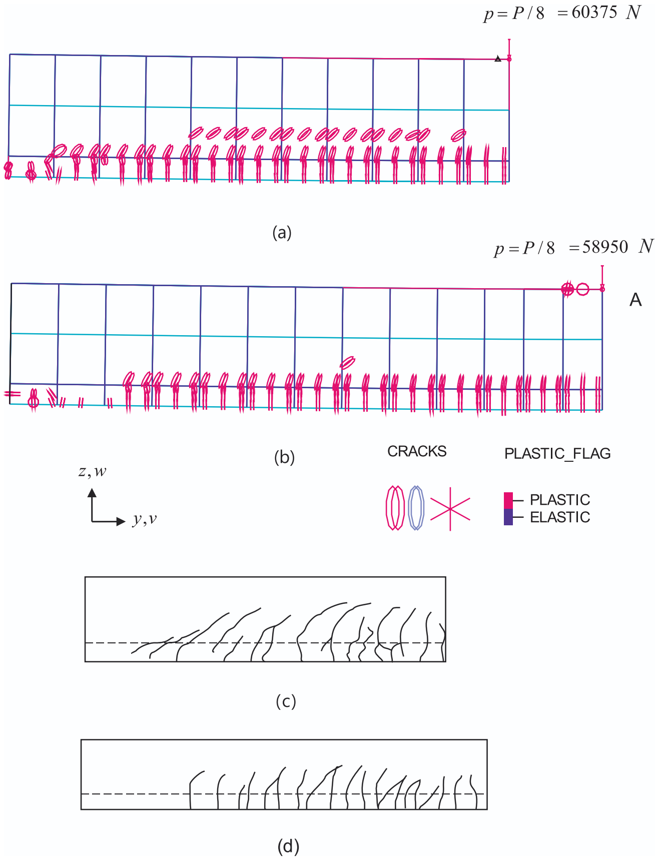

Fig. 17. Crack patterns for the shear- compression (A-2) and flexure-compression (A-3) beams at failure. Predictions using our concrete model for the (a) A-2 and (b) A-3 beams. Typical experimental patterns measured for the (c) A-2 and (d) A-3 beams (B Bresler and AC Scordelis [51]).

relevant update to the constitutive matrix in Eqs. (30), (31) lead to an efficient solution scheme, see Appendix C for more details. By using the consistent stress–strain matrix, the solution can reach a quadratic convergence rate.

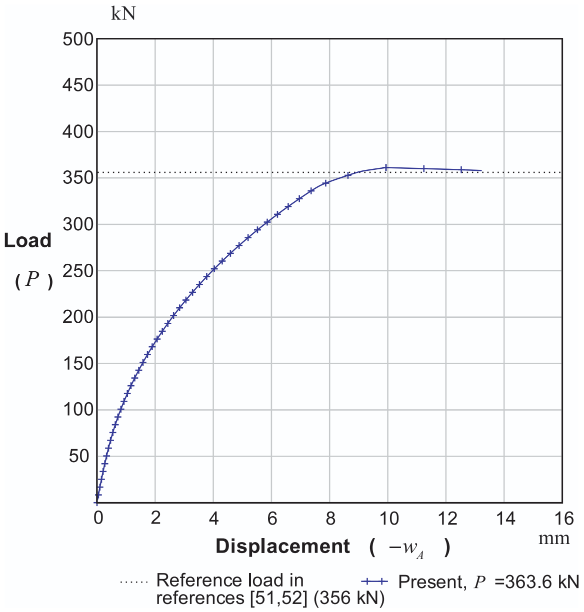

Fig. 18. Calculated load–displacement curve of the OA-2 beam.

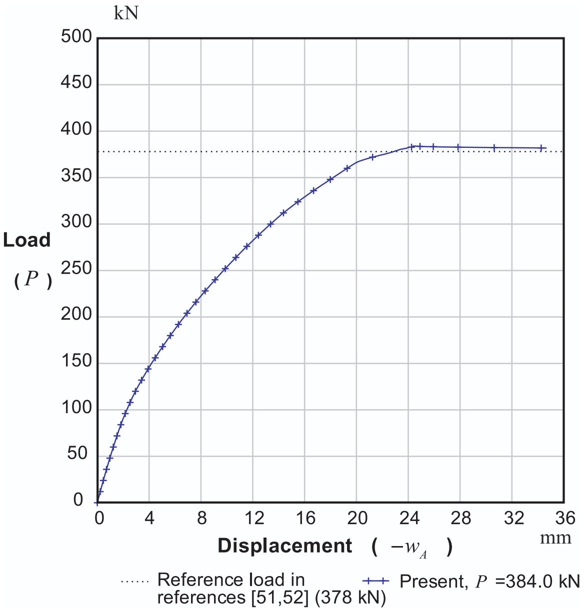

Fig. 19. Calculated load–displacement curve of the OA-3 beam.

Table 8
Comparison of ultimate loads of Scordelis-Bresler beams.

Beams	Present P_u	Ultimate loads (P) in kN Experiment $P_{u-\exp}$[51,52]	 Theory $P_{u-theor}$[51,52]	$P_u/P_{u-theor}$ $(P_{u-\exp}/P_{u-theor})$
A-2	483.0	489	423	1.14 (1.16)
A-3	471.6	467	414	1.14 (1.13)
OA-2	363.6	356	292	1.25 (1.22)
OA-3	384.0	378	293	1.31 (1.29)

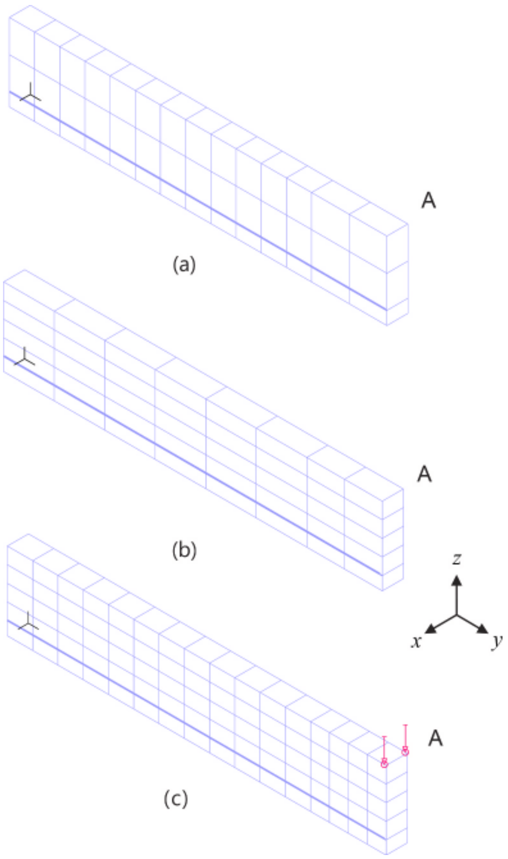

Fig. 20. Additional sensitivity study on meshes, based on OA-3 beam (G_F = 0.46 N/mm). (a) Refined mesh A (l_b = 210 mm). (b) Refined mesh B (l_b = 255 mm). (c) Refined mesh C (l_b = 240 mm).

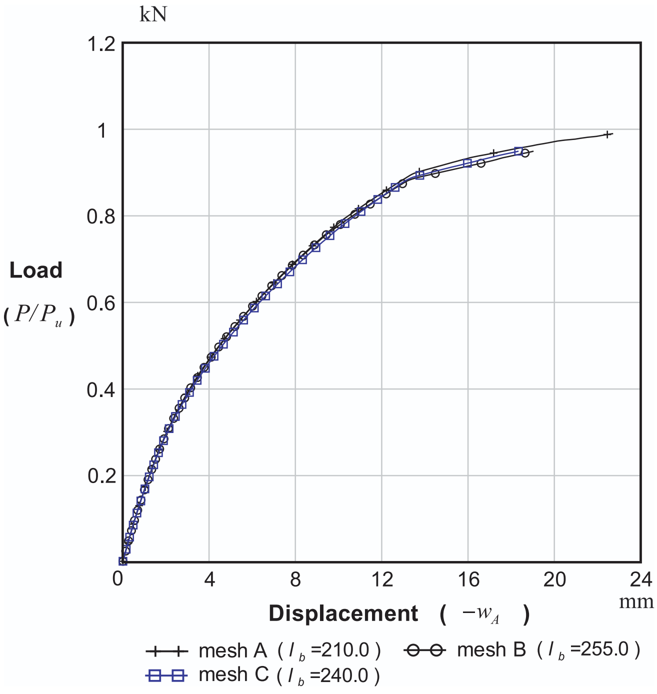

Fig. 21. Sensitivity study to mesh refinement, OA-3 beam.

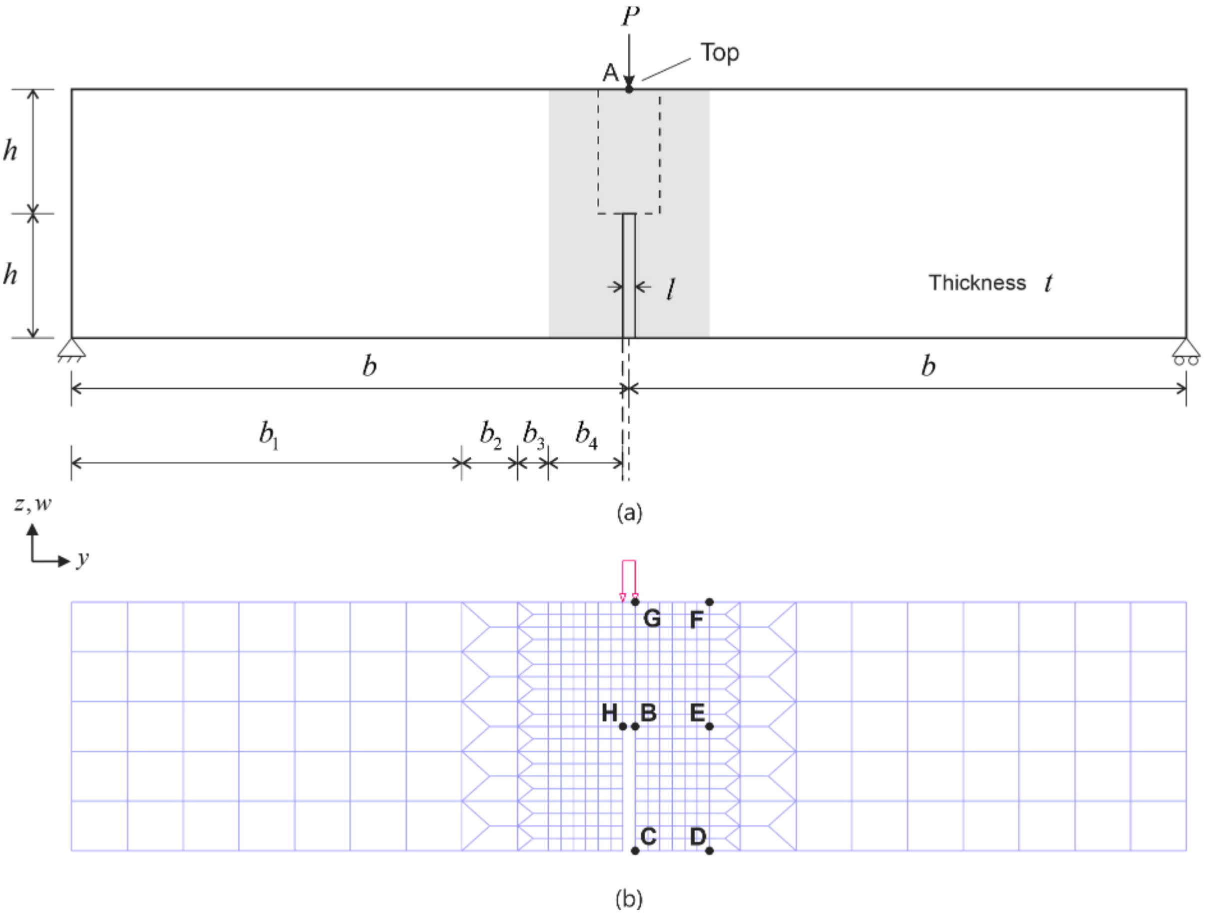

Fig. 22. The notched beam in bending. (a) Problem definition ($h = 100\,\text{mm}, t = 100\,\text{mm}, b = 225.0\,\text{mm}, l = 5.0\,\text{mm}$). (b) Finite element idealization with lengths of coupling zones ($b_1 = 157.5\,\text{mm}, b_2 = 22.5\,\text{mm}, b_3 = 12.5\,\text{mm}, b_3 = 30.0\,\text{mm}$) shown with reference mesh.

Table 9
Input parameters for the notched beam.

Parameters from the present model
f_c, t_p (0.10), $G_F = 0.090\,\text{N/mm}$, $E = 2.0 \times 10^3\,\text{MPa}$, $\nu = 0.2$,l_b

The solution procedure tests whether the material is in compression or tension, whether the material is loading or unloading, and whether there are cracks or we have a crushed state, see Table 1. We demonstrate the solution scheme in the analysis of challenging nonlinear problems in Section 3.

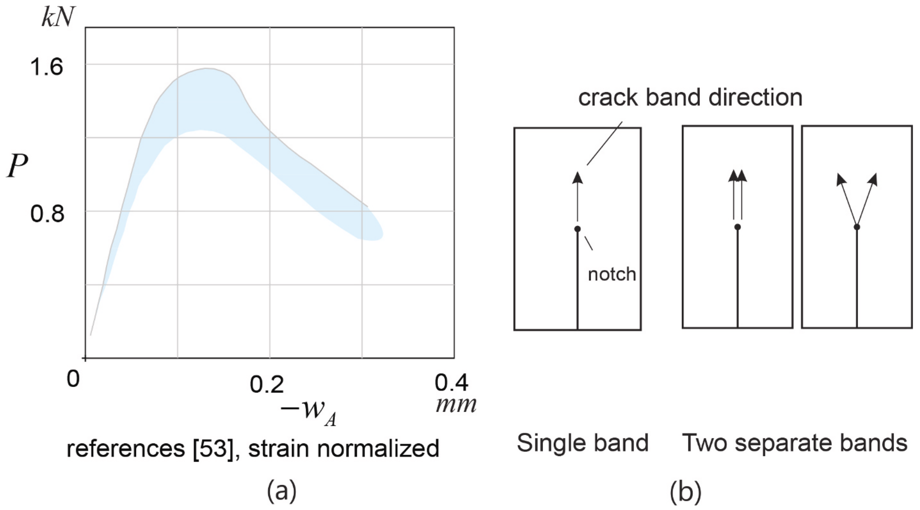

Fig. 23. Reference solution and crack growth patterns for the bending of notched beam. (a) Experimental range of solutions. (b) Localized crack growth.

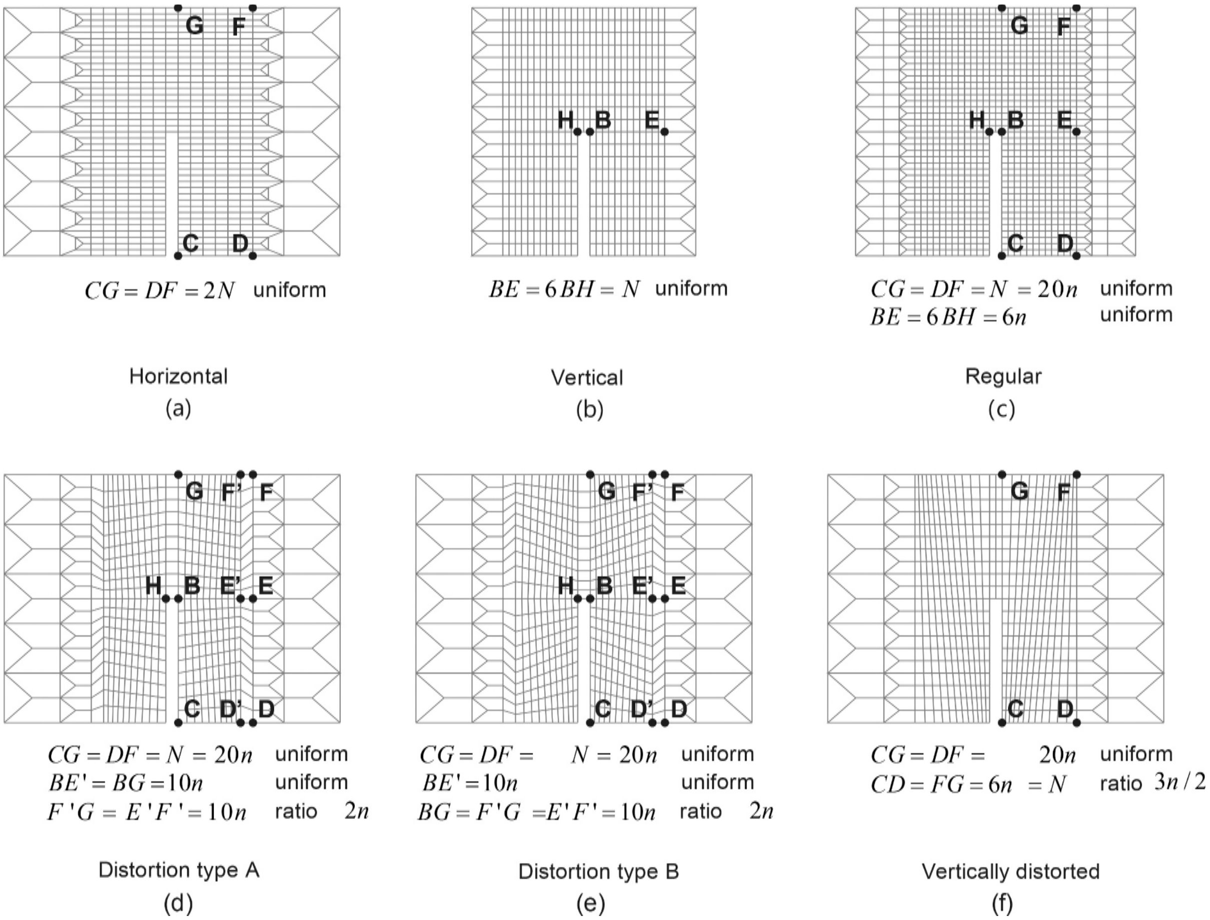

Fig. 24. The finite element mesh cases. (a) Horizontal, (b) vertical, (c) regular, (d) type A distorted, (e) type B distorted, (f) vertically distorted meshes. When an edge AB having endpoints A and B is subdivided by n with a ratio k, it is divided into n sub-edges having length ratios $AB_1 : AB_2 : \ldots : AB_n = 1 : 2 : \ldots : k$.

2.3. Implementation of solution procedure

In this section we consider the implementation of our procedure of the material model as well as its efficiency and stability. The procedure derived in Section 2.2 is presented in a concise flowchart, as shown in Fig. 8.

The difference with the procedure in [32] is that internal strains are not divided into plastic and fracture components. Instead, we maintain only the plastic strain. The fracturing is included without material iteration but instead using a change in the instantaneous state. Another difference from the conventional stress-based approach is that we do not need to repeatedly compute the stress from the strain during plasticity, as all derivatives and flow directions are measured in terms of strain.

Regarding the plasticity solution loop, it requires a simple built-in yield function $\boldsymbol{F}$ on the strain space that directly gives all coefficients and renders the procedure to be stable. The local-solution stability (solvability in the material iteration so that an iterative solution is obtained for all ranges of strains) can be assessed from the properties of the yield function, see Appendix C. The use of the principal system accounts for all six different states of strain and stress in three equations and hence is efficient.

The material model and the solution procedures have been implemented in ADINA, version 25.0 of Bentley Systems, Inc. [46]. We next give some illustrative solutions using the model and procedures.

3. Illustrative solutions

In this section we illustrate the use of our proposed concrete model. We show the predicted response in basic tests, solve a two-dimensional shear wall problem, three-dimensional reinforced concrete beam problems, and a three-dimensional dam problem. The problems considered are chosen to encompass various response possibilities that can occur in practical analyses. We summarize in Table 2 the input parameters for the present material model. Across analyses, 20-node 3D solid or 8-node 2D solid elements are employed for modeling the concrete structures.

3.1. Basic tests of model behavior

We perform uniaxial and biaxial tests. In both tests a cube is subjected to single or two compressive pressure loads with minimum boundary condition to prevent rigid body motion.

In uniaxial tests, the values obtained in P Desayi and S Krishnan [47] with $f_c = 21$ and $f_c = 30$ are used while the strains are renormalized by a multiplication factor of 2.3 to show strain values using the same scale.

The problem definition and the response of uniaxial compression are shown in Fig. 9. The present material model exhibits the correct value of critical strength across different cylindrical strengths, a behavior also found in experiments [47]. Our concrete model passes the uniaxial compressive strength test.

The problem definition and the response in biaxial compression are shown in Fig. 10. In our material model and the reference data, the stress–strain data for biaxial compression with $f_c = 32$ is used. In the reference results given by H Kupfer, HK Hilsdorf, and H Rusch [42], we used the normalized strain (e/e_{crit}) where $e_{crit} = 0.0025$, in both cases of ratios $\sigma_{zz} : \sigma_{xx} = 1 : 1$ and $\sigma_{zz} : \sigma_{xx} = 1 : 0$.

The calculated values of the critical loads for the biaxial cases are in close agreement with the experimental results in H Kupfer, HK Hilsdorf, and H Rusch. Our material model exhibits approximately a 15 %

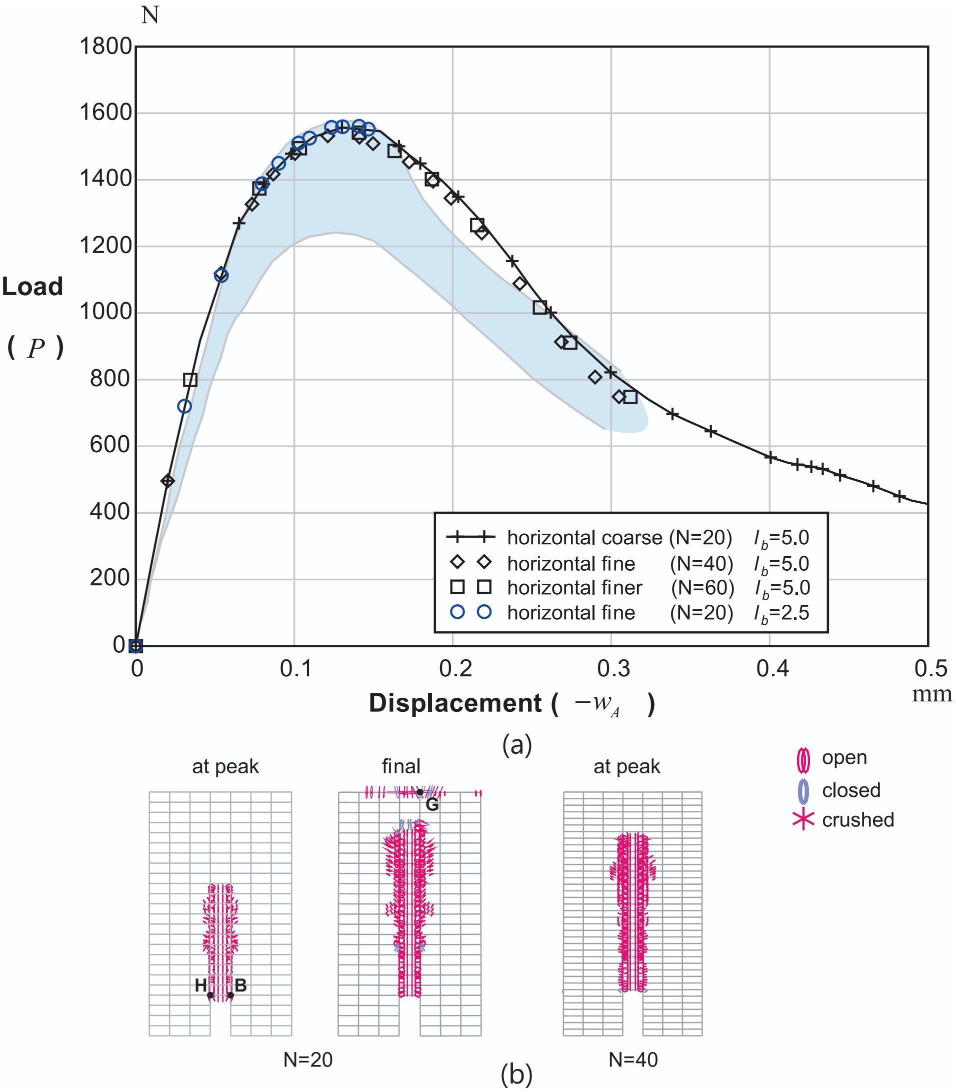

Fig. 25. The response of the notched beam in bending using the horizontally aligned meshes in Fig. 24(a). (a) The load–displacement curves. (b) A comparison of crack evolutions.

increase in strength in biaxial compression.

3.2. Analysis of concrete panel

We consider a concrete panel (W-2) subjected to a center load in Fig. 11 [48,49,50]. Half of the panel is modeled, and the reinforcing steel is idealized as rectangular elements with smeared properties and varying thicknesses in the horizontal and vertical directions. Further modeling details are presented in Tables 3 and 4. Smeared reinforcement approach is used [48–50]. For this two-dimensional problem we test our material model by using two different values of G_F in the local ($l_b = 0.0$) formulation to model cracking.

Fig. 12 shows the load–displacement curves for the W-2 wall, analyzed with monotonically increasing load. The limit load reached by the structure is studied experimentally by V Cervenka and KH Gerstle [48] and analytically by D Darwin and DA Pecknold [49]. For both cases of fracture energies, the ultimate load reached by the structure is close to the reference limit load (120 kN). The structural limiting behavior is affected by cracking, so a change is observed for the two different G_F values, but the two cases of fracture energy did not produce significantly different results.

The predicted pattern of cracks presented in Fig. 13 follows closely the experimental results. As a small difference compared to the numerical result in [50], we did not obtain crushing at the top left section of the wall but obtained instead multiple cracks at the bottom right corner of the wall.

3.3. Reinforced concrete beam problems

We present the use of our material model in the analysis of the reinforced concrete beam problems considered by B Bresler and AC Scordelis [51,52]. The ultimate load is defined as the maximum load carrying capacity reached in the nonlinear concrete behavior, cracking, and failure in reinforcements.

The beams are shown in Fig. 14 [51,52]. The beams supported at their ends are subjected to a center load. According to different geometry patterns, material properties and reinforcement conditions, the physical problems are known to exhibit different failure modes: shear-compression for the A-2, flexure-compression for the A-3, and diagonal tensile failure modes for the OA-2 and OA-3 beams [51,52]. All stiffeners are modeled separately with trusses in addition to the concrete using solid elements. The A-2 and A-3 beams contain vertical stiffeners. Tables 5–7 give details of the modeling and material properties. The analyses are performed with monotonically increasing loading under load-control, using the low-speed dynamics (quasistatic) option [46] to solve slightly past the critical point. The fracture energy $G_F = 0.46$ N/

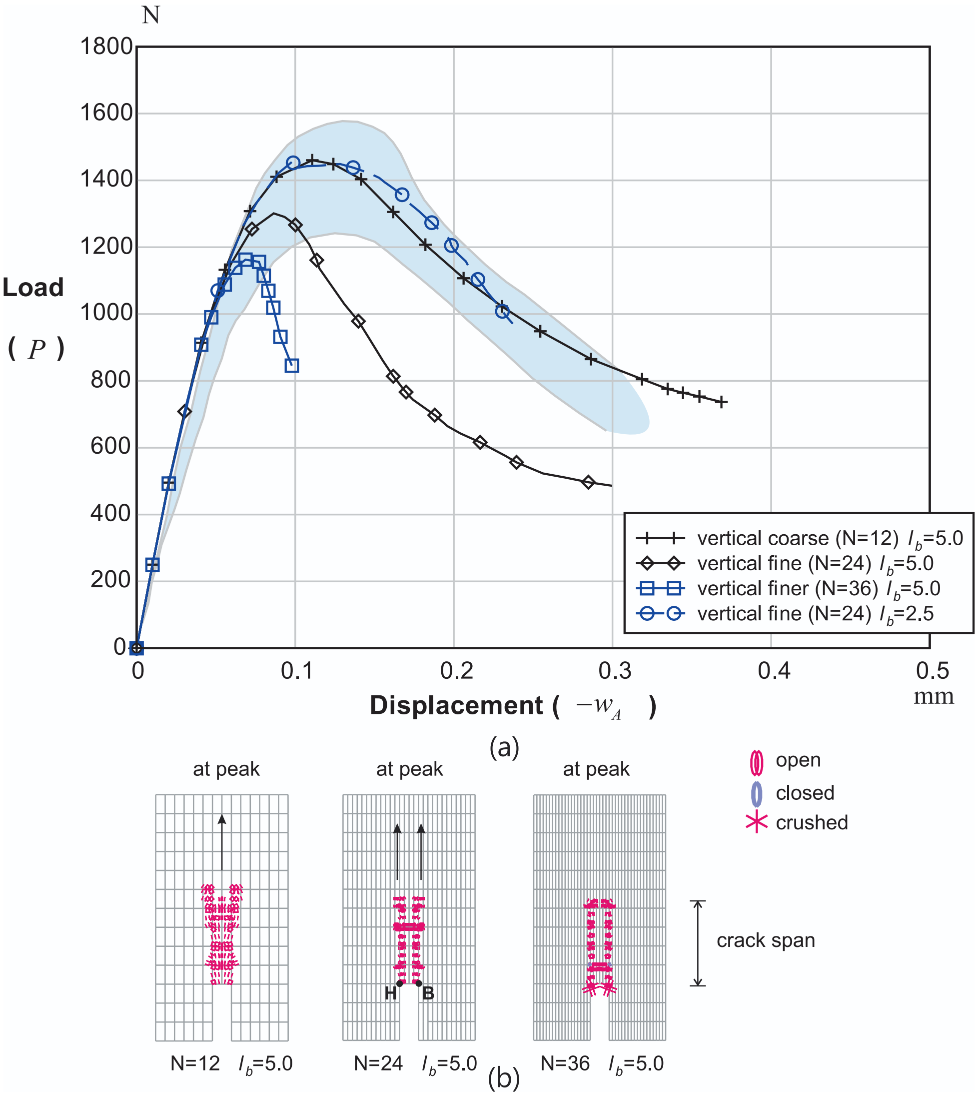

Fig. 26. The response of the notched beam using the vertically aligned meshes in Fig. 24(b). (a) The load–displacement curves. (b) A comparison of crack evolutions.

mm per unit area was prescribed, and the local interpretation of the energy on the length scale ($l_b = 0.0$) is initially used.

For the shear- and flexure-compression failure beams (A-2,A-3), Figs. 15–16 give the load–displacement curves, and Fig. 17 shows the crack patterns. These A-2 and A-3 beams reached in the experiments their ultimate load capacities mainly due to cracking, before the load–displacement behavior completely levels off [51,52]. In the solutions using our material model, the analyses of the A-2 and A-3 beams continued up to the point of the top reinforcement reaching the yield point and cracks permeated from the bottom, see [51]. The crack patterns at the ultimate load, including for the A-2 beam, show more cracks aligned toward the center of the beam near the cracked end, which is in good agreement with the experimental patterns in B Bresler and AC Scordelis [51]. The ultimate loads reached (493.0 kN;471.6 kN) compared well with the experimental reference loads (489 kN;467 kN) given in Refs. [51,52] for the (A-2,A-3) beams, respectively.

Figs. 18-19 give the load–displacement curves for the beams failing in diagonal tensile failure (OA-2,OA-3). The ultimate loads reached in our analyses (363.6 kN;384.0 kN) are also close to the experimental reference loads (356 kN;378 kN) in Refs. [51,52]. Further comparisons of the ultimate load predictions are given in Table 8 [51,52].

In addition, we choose the tensile-diagonal failure beam (OA-3) and provide mesh refinement studies in Figs. 20-21. This structure fails in mixed compression and tension, and the ultimate load depends upon not just the strength of the material but also the energy absorbed by the crack. For the cracking part, the global manual inputs of l_b are given in Eq. (22) in an attempt to regularize the sensitivity. The Fig. 21 shows that for the meshes considered, the attained load–displacement curves are nearly the same. Detailed rules for determining l_b are discussed in the next example with a relatively simpler tensile dominant failure.

3.4. Notched beam under bending

We analyze a notched beam under three-point bending, see Fig. 22 [45,53] and Table 9. A beam of length $2b$, height $2h$ and thickness t is subject to bending load at the top surface above the notched crack of width l and depth h. Concrete beams of this specific size and shape were investigated experimentally by HA Kormeling and HW Reinhardt [53] and simulated in [54–57]. To match the material properties, $f_t = t_p \times f_c = 2.4\,\mathrm{MPa}$ with $t_p = 0.10$ and $f_c = 24\,\mathrm{MPa}$ were employed with additional initial modulus $E = 2.0\,\mathrm{GPa}$ and $\nu = 0.2$.

The fracture energy $G_F = 0.090\,\mathrm{N/mm}$ per unit area was normalized by characteristic length scale l_b, which should be given from the width of the crack band. This depends upon detailed factors such as formulation, problem definition, and the finite element utilized [45]. For testing the global interpretation of crack energy, we initially select the length scale to be the same as the width of the notch $l_b = l = 5\,\mathrm{mm}$ from the

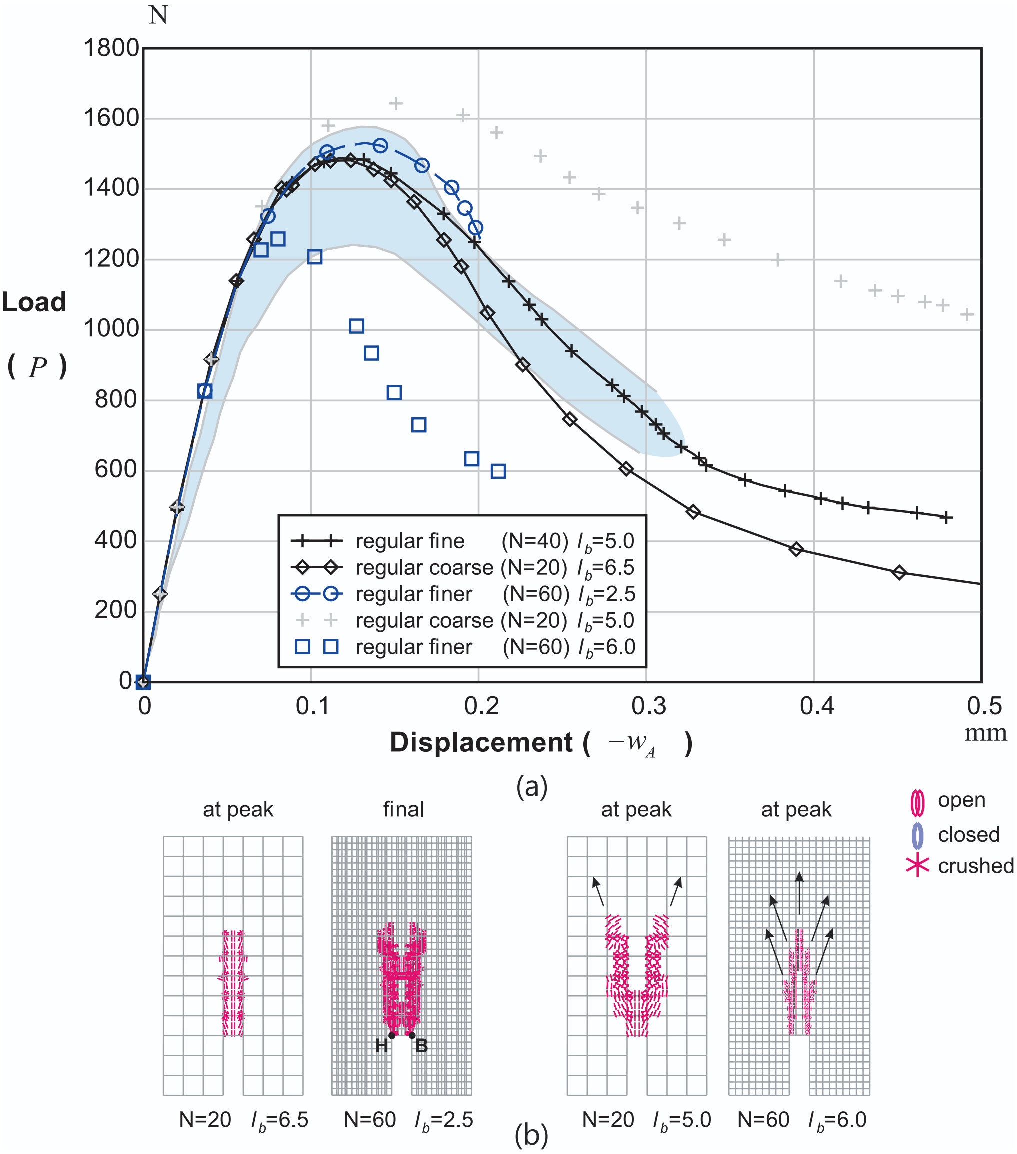

Fig. 27. The response of the notched beam in bending using the regular meshes in Fig. 24(c). (a) The load–displacement curves. (b) A comparison of crack evolutions.

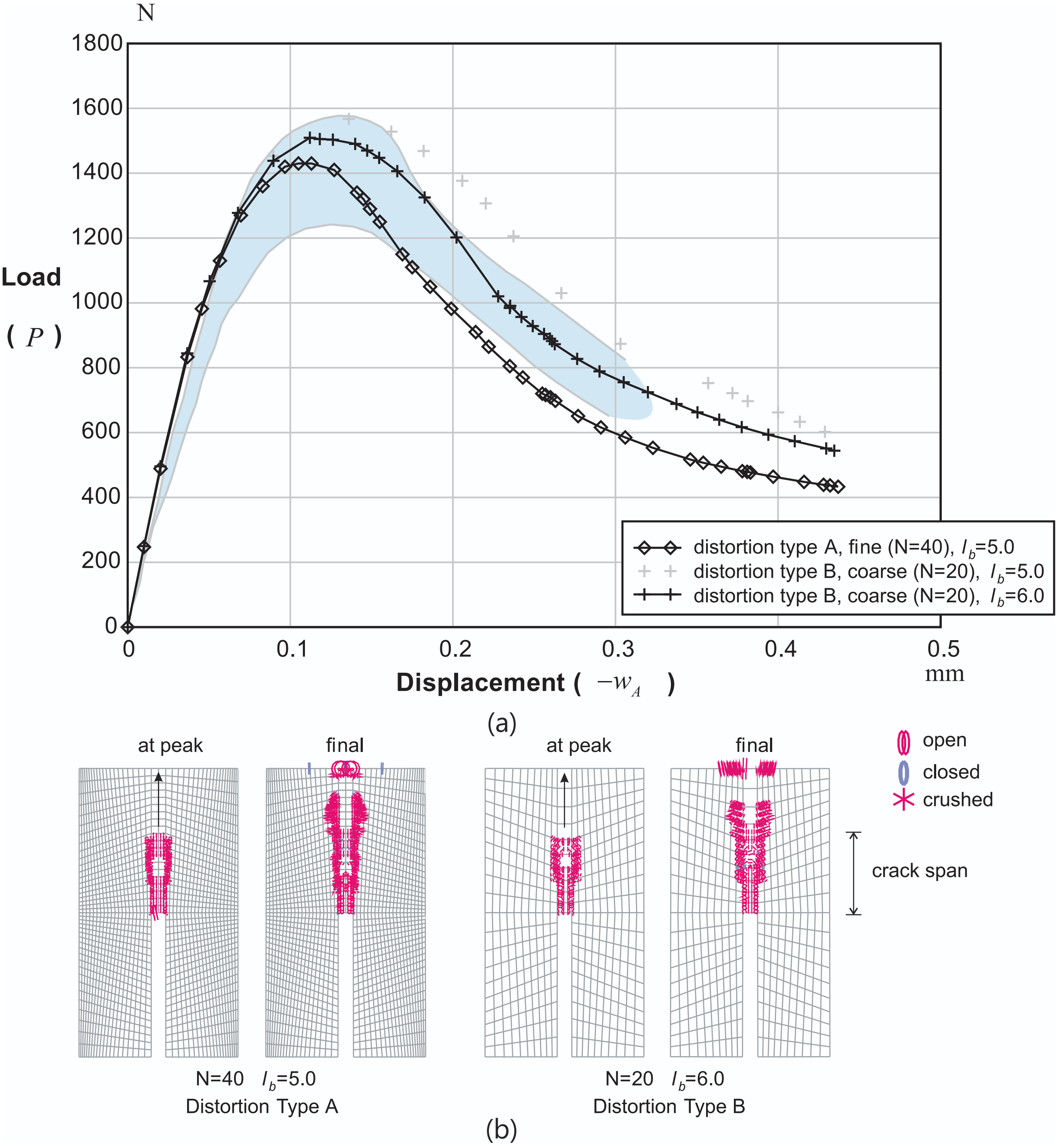

Fig. 28. The response of the notched beam in bending using the distorted meshes in Fig. 24(d) and 24(e). (a) The calculated load–displacement curves. (b) A comparison of crack evolutions.

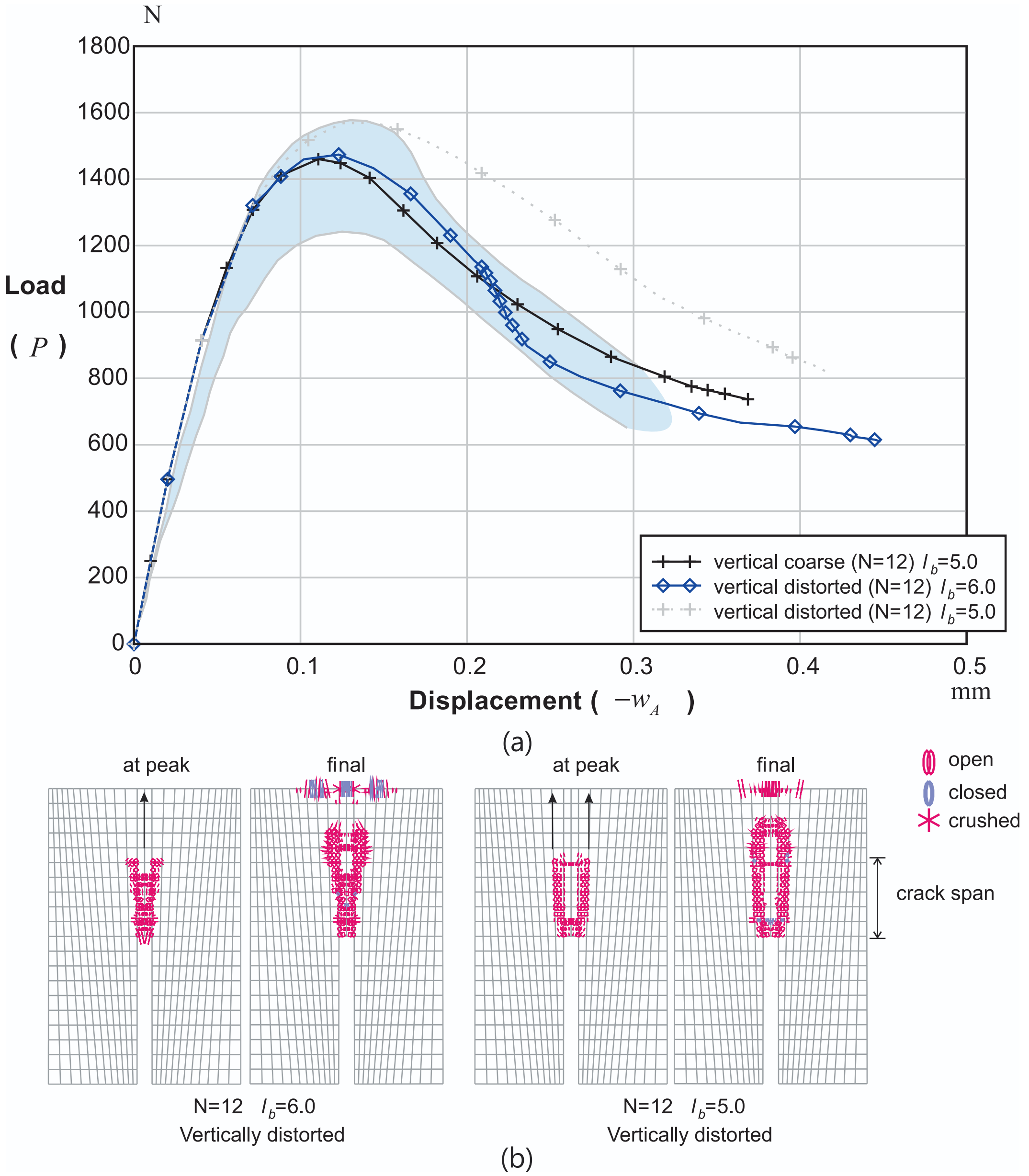

Fig. 29. The response of the notched beam in bending using the vertically aligned meshes with distortions in Fig. 24(e). (a) The calculated load–displacement curves. (b) A comparison of crack evolutions.

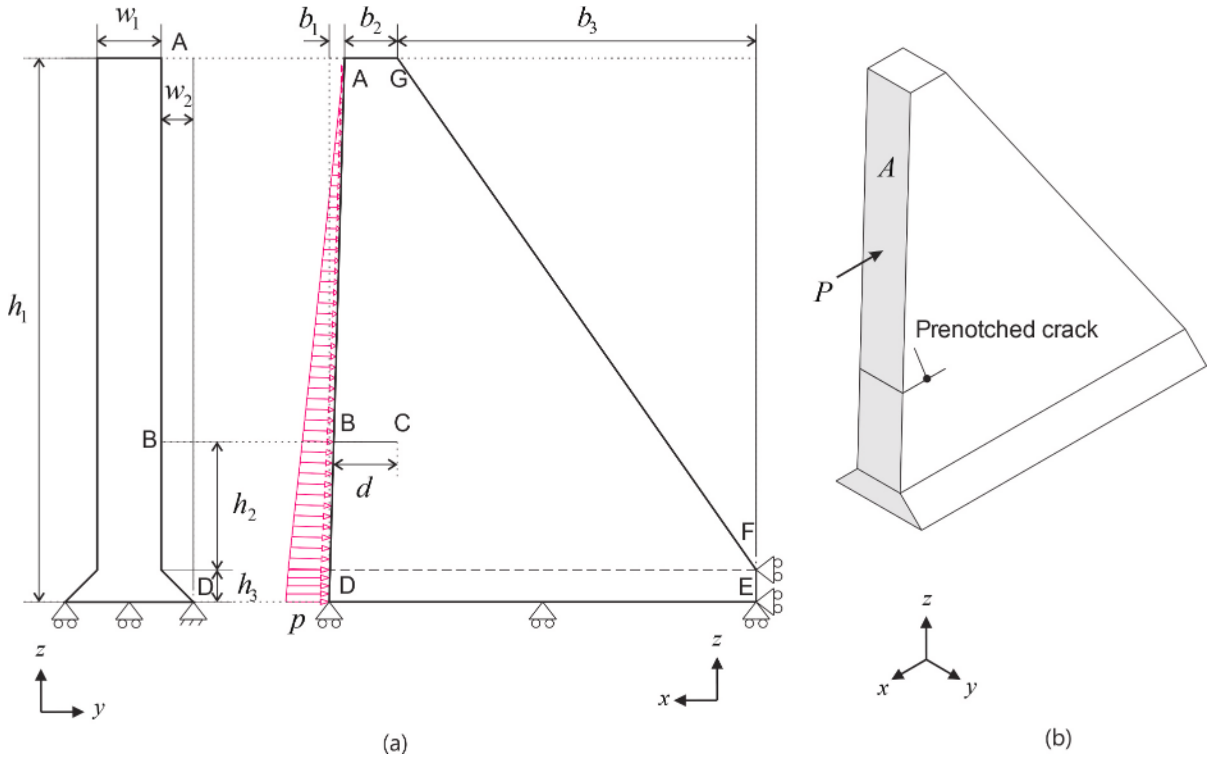

Fig. 30. Gravity dam problem. (a) Problem definition (geometry $b_1 = 72\,\text{mm}, b_2 = 248\,\text{mm}, b_3 = 1680\,\text{mm}, d = 300\,\text{mm}, h_1 = 2550\,\text{mm}, h_2 = 600\,\text{mm}, h_3 = 150\,\text{mm}, w_1 = 300\,\text{mm}, w_2 = 150\,\text{mm}$; pressure $p = 3.137\,\text{N/mm}^2$; concrete properties $f_c = 36\,\text{N/mm}^2$, $G_F = 0.184\,\text{N/mm}$). (b) Prenotched crack (emanating at B from the shaded section area A). The total applied load is $P = \int_A p dA = 1337\,\text{N}$ per unit load step. Dimensions in [mm, N, MPa].

Table 10
Input parameters for the dam.

Parameters from the present model
f_c, t_p (0.05), G_F (0.184 N/mm), $l_b = 120\,\text{mm}$

geometry of the structure.

The reference range of the load–displacement curves shown in Fig. 23(a) is taken from the experimental results in [53], where we apply the value 1.3 in strain to match the strain on the same scale. The reference peak load occurs at 1.2 to 1.6 kN. The reason for the multiplication is that our material utilizes specific material constants taken from the literature (as critical strain locations), see Appendix C. Analyses are performed with load–displacement control [36,46] to obtain the response with softening.

In this problem, the crack grows from the end of the notch and emanates vertically and also toward the beam ends, forming a crack zone, which is shown by the shaded area in Fig. 22(a). To identify the effect of meshing in the crack zone, we perform convergence studies with the different meshes given in Ref. [45], and also use distorted mesh patterns as given in Refs. [58,59]. Fig. 24 gives an overview of the finite element meshes used. Two potential crack scenarios occur as shown in Fig. 23(b) considering local effects, but the correct global pattern is a single crack band in Mode I failure.

Fig. 25 presents the load–displacement curves using the horizontally aligned mesh. The results from horizontally refining the mesh gave the same result as obtained without the refinement and were in good agreement with the experimental range.

Fig. 26 gives the load–displacement curves using the vertically aligned mesh. Unlike when using the horizontally aligned mesh case, the length scale input had to be refined. For the vertically aligned meshes, local effects in Fig. 23(b) dominate, so we apply Fig. 7(b) to determine the crack width l_b from the element length,

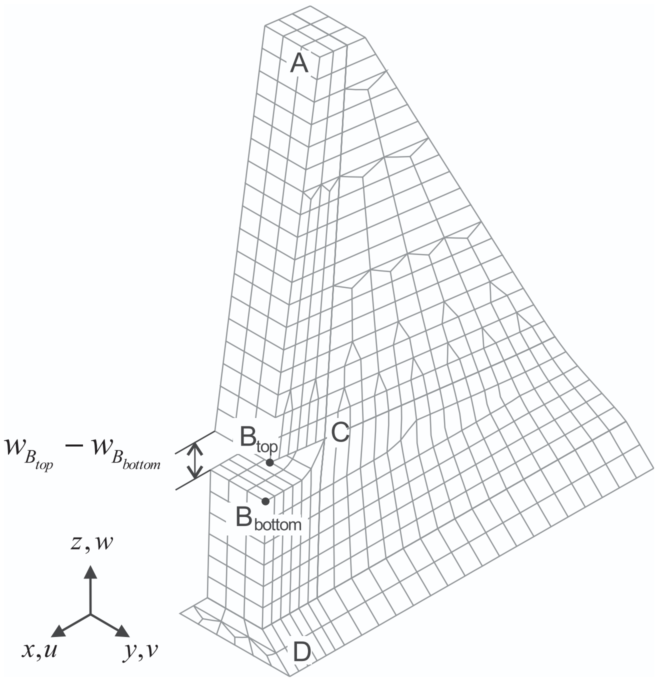

Fig. 31. Deformed shape of the dam, also showing the crack opening relative displacement at B.

$$l_b = l/n \tag{32}$$

where n is the number of elements within the notch of width l.

Then the results lie within the experimental range across different mesh refinements.

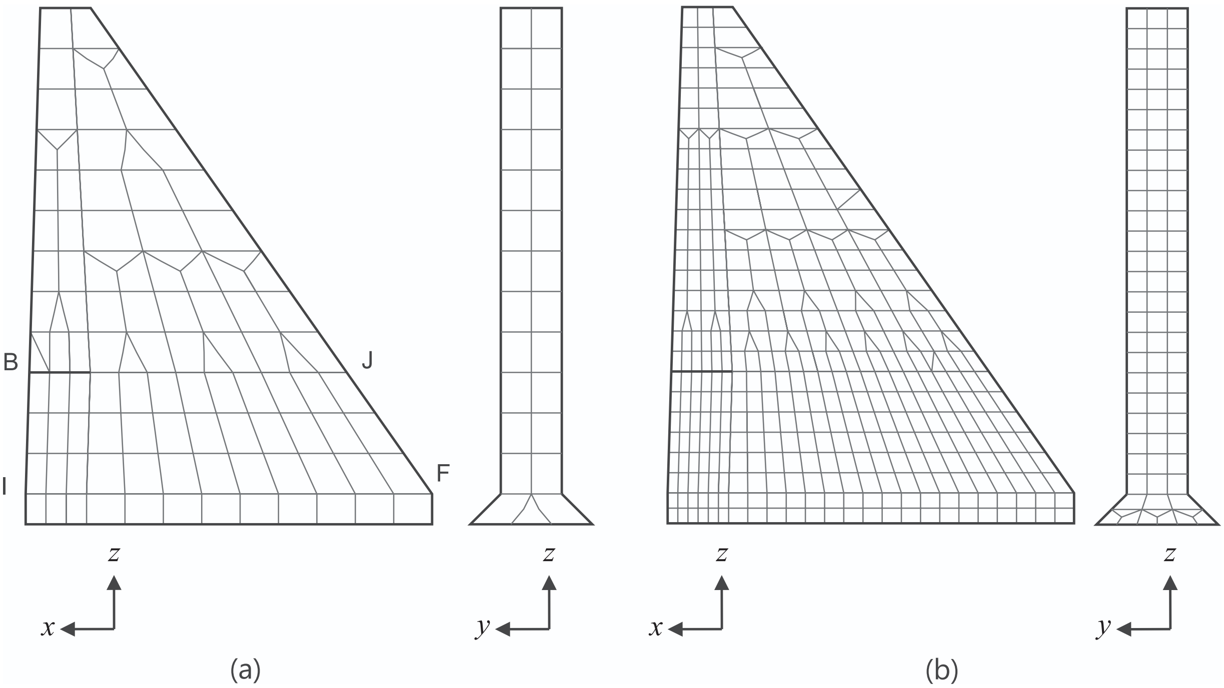

Fig. 32. Meshes used for the dam problem, (a) the coarse mesh, (b) the fine mesh.

Fig. 27 shows the load–displacement curves when using the regular meshes. To mitigate the effect of the occurrence of two crack bands in Fig. 23(b), the regular mesh cases required l_b to be increased. From the crack coalescence experiment in Ref. [65], the percentage of load applied to merge two cracks with low bridging angles in each band is 20 %–25 %. When two parallel cracks are merged, the fracture energy in the combined crack is reduced to a smaller value of 75 % to 80 %

$$g_F = G_F/l_b \tag{33}$$

For a normalized facture energy g_F, and an initial value $l_b = 5.5$ mm, the values of l_b to represent the correct reduced crack energy after the coalescing of the two parallel cracks are $l_b = 6.0$ mm to $l_b = 6.5$ mm. Using these values, the solutions following the single crack band pattern in Fig. 23(b) showed good agreement with the experimental range.

Fig. 28 shows the load–displacement curves using the distorted mesh cases in Fig. 24(d) and (e). It is possible to apply the regularization to obtain good responses also when using the distorted meshes with nearly equal side lengths. Using the Type B distorted mesh results in better results than using the Type A mesh, requiring less mesh density in the solution.

Fig. 29 shows the load–displacement curves using the distorted mesh in the vertically aligned setup. Mesh alignments induce the crack to spread out as in the localized crack growth in Fig. 23(b). With the length scale adjusted again with Eq. (33) to capture the wider crack band growth in the distorted mesh, the response agrees well with the results using the undistorted mesh and is within the experimental range.

In summary, we applied the crack-band approach to determine the element length [22,30,45] for our solution and performed convergence and mesh sensitivity studies. It is shown that the predicted response can be regularized to a reference solution irrespective of the mesh size, element aspect ratios, or distortions present in the mesh using a single parameter l_b.

3.5. *Gravity dam problem*

We analyze a gravity dam with an initial crack subjected to hydraulic loading, see Fig. 30 [60,61] and Table 10. The experiment was performed by Carpinteri et al. [60] on a 1:40 scaled-down model, and the model was analyzed extensively in different studies [61]. A section of the dam is subjected to hydrostatic loading and local crack opening and closure can take place, see Fig. 31. The boundary conditions are $w = 0$ at the bottom surface DE, $u = 0$ at the back surface FE, and $u = v = w = 0$ at point D. The coarse and fine meshes used for the response predictions are shown in Fig. 32.

The crack mouth opening displacement is obtained through a solution using the load–displacement control (LDC) scheme with line searches [36,46]. The load–displacement curves are shown in Fig. 33. When using the load–displacement control with line searches and the fine mesh, our material model shows excellent agreement with the experimental result. The resulting crack bands are shown in Fig. 34. The crack band occurs in the region beneath the notch, forming a positive angle from the horizontal direction. The tangent angle obtained using for the solution the load–displacement control with line searches is greater than when only using the load–displacement control, and also the resulting band is straighter, demonstrating the better accuracy of the solution. In the converged solution from the mesh refinement, the width of the slanted crack band is shown to be 120 mm, which agrees with our choice of length scale l_b described in Fig. 7.

4. Concluding remarks

We proposed a new concrete material model for finite element analysis. The phenomena of fracture and cracking are merged into a new plastic solution procedure (to model the compression effects) with flow rules separately derived and used for three independent failure surfaces used in a compression coordinate system. The coupling between plasticity and fracture of the phenomenological behavior of concrete is introduced using the material strains represented in their principal coordinates. The concrete material model is embedded in a generally applicable and effective finite element solution procedure, with the only assumption (usually satisfied) that the constitutive relationship is calculated locally at the integration points.

The proposed material model shows the empirical limiting behaviors following the ultimate strength of the concrete considered and tensile failure with cracking and tension-stiffening effects. The numerical predictions reached illustrate the capability of the material model to

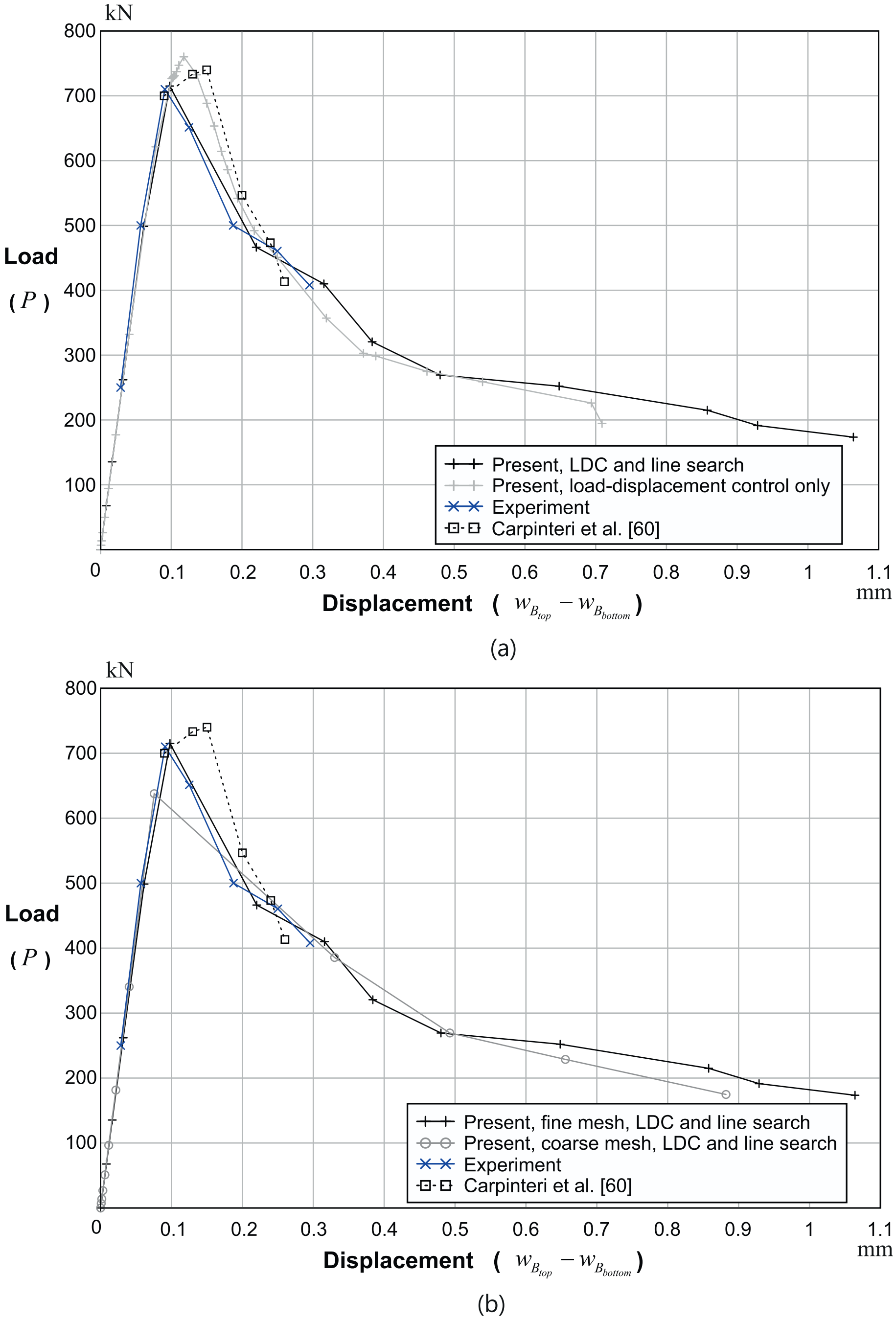

(a)

(b)

Fig. 33. Load-displacement curves of the gravity dam, considering (a) LDC with or without line-searches, (b) mesh refinement.

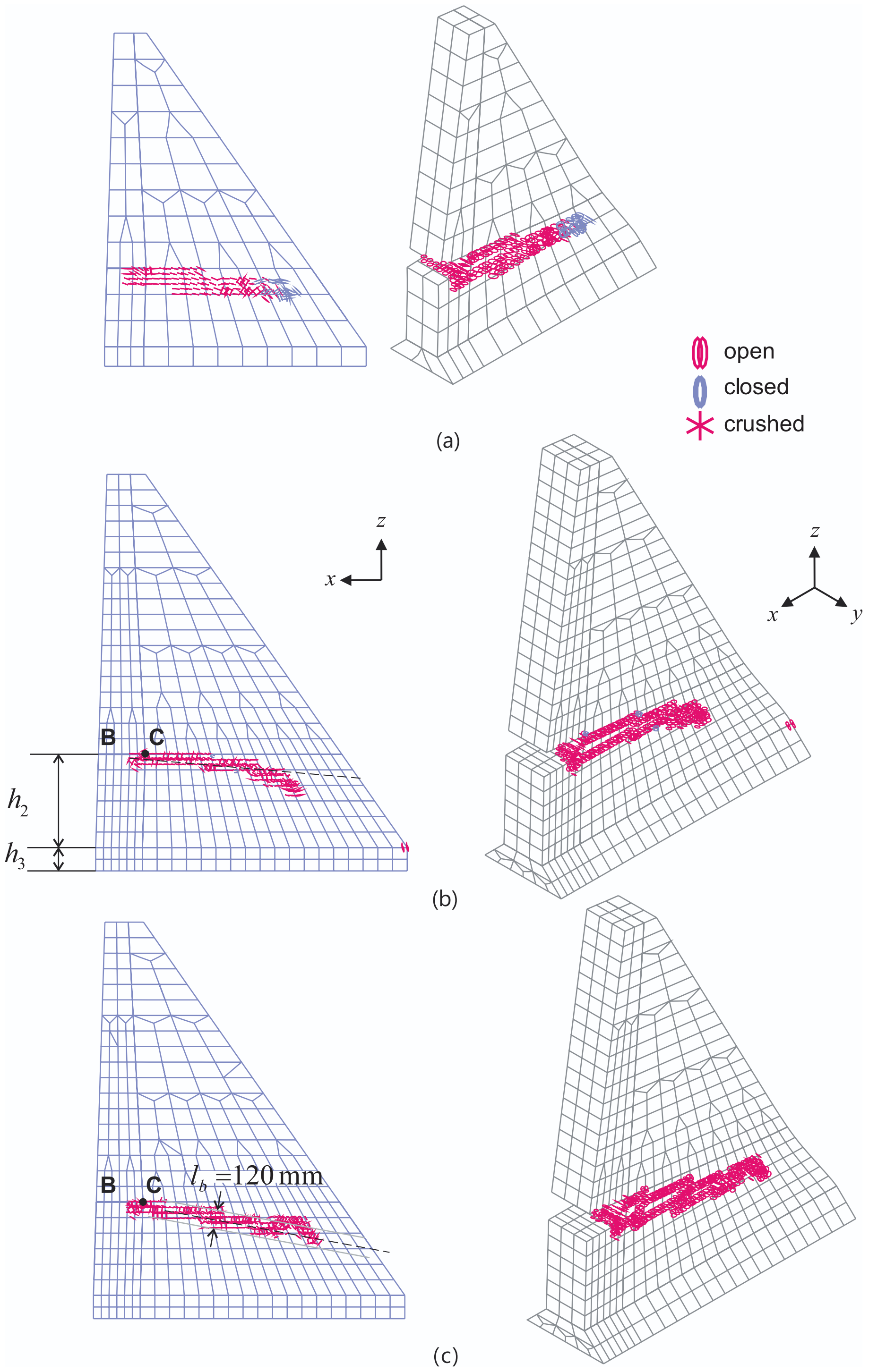

Fig. 34. Crack bands of the gravity dam, solutions obtained with (a) the coarse mesh, (b) the fine mesh using LDC only, and (c) the fine mesh using both LDC and line searches. The left and right columns indicate the original and magnified deformed configurations, respectively.

simulate concrete behavior in challenging analysis problems with high nonlinearities that include crushing and cracking of the concrete and the effects of reinforcements.

While the numerical results illustrated the capability of the material model to represent concrete behavior in some challenging analysis problems with complex nonlinearities, we only used the concrete model in the analyses of some, although varied, problems and employed specific experimental forms and material constants published earlier [31,39–44]. The coefficients from Refs. [39–43] might be outdated. Hence, extending the material input parameters in our material model to handle these and the use of different built-in equations and coefficients needs to be studied.

However, we can conclude that our proposed solution procedure is already valuable and also represents “an avenue” with good potential to reach an “all-encompassing scheme” to simulate complex nonlinear behavior of concrete structures including failure. A study of the wider applicability of our concrete model, in particular, in different modes of failure, e.g. see Refs. [62,63], is envisaged for the future.’

CRediT authorship contribution statement

Yeongbin Ko: Writing – review & editing, Writing – original draft, Validation, Methodology, Investigation, Formal analysis, Conceptualization. **Klaus-Jürgen Bathe:** Writing – review & editing, Supervision.

Declaration of competing interest

The authors declare that they have no known competing financial interests or personal relationships that could have appeared to influence the work reported in this paper.

Appendix A. Experimental fits of moduli using f_c in Eqs. (9c), (10), (11) and crack strength in Eq. (16)

When just compressive cylindrical strength f_c was specified without E or ν, initial bulk and shear moduli are determined from experimental fit. All data are given in units [MPa].

$$\begin{aligned} K_e &= 11000 + 3.2 f_c \\ G_e &= 9224 + 136.0 f_c + 3296 \times 10^{-15} f_c^{8.273} \end{aligned} \tag{A.1}$$

The coefficients used in Eqs. (10), (11) are,
if $f_c \leqslant 31.7$

$$A = 0.516,\ c = 3.573,\ d = 2.12 + 0.0183 f_c,\ m = -2.415,\ n = 1.0, \tag{A.2}$$

and if $f_c > 31.7$

$$\begin{aligned} &A = 0.516/(1 + 0.0027(f_c - 31.7)^{2.397}),\ c = 3.573/(1 + 0.0134(f_c - 31.7)^{1.414}), \\ &d = 2.7,\ m = -3.531 + 0.0352 f_c,\ n = -0.3124 + 0.0217 f_c, \end{aligned} \tag{A.3}$$

In addition we have for all f_c

$$\begin{aligned} &b = 2 + 1.81 \times 10^{-8} f_c^{4.461},\ k = 4/(1 + 1.087(f_c - 15)^{0.23}) \\ &l = 0.222 + 0.01086 f_c - 0.000122 f_c^2 \end{aligned} \tag{A.4}$$

When calculating the strength envelope for cracking, we use only the three constants f_c, t_p, and G_F in Eq. (16) following Refs. [31,44] and shown in Fig. 1. The tensile strength is given by $f_t = t_p \cdot f_c \in [0.05 \cdot f_c, 0.10 \cdot f_c]$.

Appendix B. Equivalence of Eqs. (13e)–(14a), (14b)

We use the identities

$$\begin{aligned} \cos(\frac{2\pi}{3} - \theta) &= \cos(\frac{2\pi}{3})\cos(\theta) + \sin(\frac{2\pi}{3})\sin(\theta) = -\frac{1}{2}\cos(\theta) + \frac{\sqrt{3}}{2}\sin(\theta) \\ \cos(\frac{2\pi}{3} + \theta) &= \cos(\frac{2\pi}{3})\cos(\theta) - \sin(\frac{2\pi}{3})\sin(\theta) = -\frac{1}{2}\cos(\theta) - \frac{\sqrt{3}}{2}\sin(\theta) \end{aligned} \tag{B.1}$$

$$\begin{aligned} \cos(\frac{\pi}{3} - \theta) &= \cos(\frac{\pi}{3})\cos(\theta) + \sin(\frac{\pi}{3})\sin(\theta) = \frac{1}{2}\cos(\theta) + \frac{\sqrt{3}}{2}\sin(\theta) \\ \sin(\frac{\pi}{3} - \theta) &= \sin(\frac{\pi}{3})\cos(\theta) - \cos(\frac{\pi}{3})\sin(\theta) = \frac{\sqrt{3}}{2}\cos(\theta) - \frac{1}{2}\sin(\theta) \end{aligned} \tag{B.2}$$

and also the inverse relations

$$\begin{aligned} \cos(\theta) &= \frac{1}{2}\cos(\frac{\pi}{3} - \theta) + \frac{1}{2}\sqrt{3}\sin(\frac{\pi}{3} - \theta) \\ \sin(\theta) &= \frac{1}{2}\sqrt{3}\cos(\frac{\pi}{3} - \theta) - \frac{1}{2}\sin(\frac{\pi}{3} - \theta) \end{aligned} \tag{B.3}$$

Thus we have

$$\begin{bmatrix} 1 \\ -\frac{1}{2} \\ -\frac{1}{2} \end{bmatrix}\cos(\theta) + \begin{bmatrix} 0 \\ \frac{\sqrt{3}}{2} \\ -\frac{\sqrt{3}}{2} \end{bmatrix}\sin(\theta) = \begin{bmatrix} \frac{1}{2} \\ \frac{1}{2} \\ -1 \end{bmatrix}\cos(\frac{\pi}{3} - \theta) + \begin{bmatrix} \frac{\sqrt{3}}{2} \\ -\frac{\sqrt{3}}{2} \\ 0 \end{bmatrix}\sin(\frac{\pi}{3} - \theta) \tag{B.4}$$

With Eq. (B.1) and Eq. (13e) expanded we also have

$$\begin{bmatrix} \overline{e}_1^e \\ \overline{e}_2^e \\ \overline{e}_3^e \end{bmatrix} = \frac{D_1}{3}\begin{bmatrix} 1 \\ 1 \\ 1 \end{bmatrix} + \sqrt{\frac{4D_2}{3}}\begin{bmatrix} 1 \\ -1/2 \\ -1/2 \end{bmatrix}\cos(\theta) + \sqrt{\frac{4D_2}{3}}\begin{bmatrix} 0 \\ \sqrt{3}/2 \\ -\sqrt{3}/2 \end{bmatrix}\sin(\theta) \tag{B.5}$$

Using Eq. (B.4) and Eq. (B.5), and substituting the definition of the coordinates and base vectors in Eq. (14), we obtain

$$\begin{bmatrix} \overline{e}_1^e \\ \overline{e}_2^e \\ \overline{e}_3^e \end{bmatrix} = \frac{D_1}{\sqrt{3}}\begin{bmatrix} 1/\sqrt{3} \\ 1/\sqrt{3} \\ 1/\sqrt{3} \end{bmatrix} + \sqrt{\frac{4D_2}{3}}(\frac{1}{2})\begin{bmatrix} 1 \\ 1 \\ -2 \end{bmatrix}\cos(\frac{\pi}{3} - \theta) + \sqrt{\frac{4D_2}{3}}(\frac{\sqrt{3}}{2})\begin{bmatrix} 1 \\ -1 \\ 0 \end{bmatrix}\sin(\frac{\pi}{3} - \theta)$$

$$= \frac{D_1}{\sqrt{3}}\widehat{\boldsymbol{p}}_1 + \sqrt{\frac{4D_2}{3}}(\frac{\sqrt{3}}{\sqrt{2}})\widehat{\boldsymbol{p}}_2\cos(\frac{\pi}{3} - \theta) + \sqrt{\frac{4D_2}{3}}(\frac{\sqrt{3}}{\sqrt{2}})\widehat{\boldsymbol{p}}_3\sin(\frac{\pi}{3} - \theta) = e_1^e\widehat{\boldsymbol{p}}_1 + e_2^e\widehat{\boldsymbol{p}}_2 + e_3^e\widehat{\boldsymbol{p}}_3 \tag{B.6}$$

which verifies the equivalence of Eq. (13e) and Eqs. (14a), (14b).

Appendix C. Plastic failure curves used in Eq. (15d) and their boundedness

We introduce plastic failure curves to use in calculating the strain response.

The coefficients of the functions were found from an experimental fit of the strength data in Refs. [16,39–43],

$$m_2 = 1/\ln(\sqrt{2/3}\cdot\alpha_2/(\beta_2\cdot\widehat{\varepsilon}_{p2})),\ m_3 = 1/\ln(1.15/\sqrt{2}\cdot\alpha_3/(\beta_3\cdot\widehat{\varepsilon}_{p3}))$$

$$\widehat{\varepsilon}_{p2} = 0.0012,\ \widehat{\varepsilon}_{p3} = 0.0025$$

$$e_{p2}^c = \max(0, K_e\widehat{e}_{p1} - 0.45),\ e_{p3}^c = \max(0, K_e\widehat{e}_{p1} - 2.17),\ \alpha_2 = 1 + 0.575\cdot(e_{p2}^c)^{0.315}$$

$$\beta_2 = 1 + 8.4\cdot(e_{p2}^c)^{0.25},\ \alpha_3 = 1 + 0.389\cdot(e_{p3}^c)^{0.315},\ \beta_3 = 1 + 5.95\cdot(e_{p3}^c)^{0.25},\ a = 2.5\times10^{-5},\ s = 0.8 \tag{C.1}$$

See Ref. [16] for a review, and we use in our study

$$c_2 = (\beta_2\cdot\widehat{\varepsilon}_{p2})\cdot m_2^{(1/m_2)},\ c_3 = \beta_3\cdot\widehat{\varepsilon}_{p3}\cdot m_3^{(1/m_3)} \tag{C.2}$$

$$c_{p1} = 3.0,\ c_{p2} = 36.0,\ c_{p3} = 12.0 \tag{C.3}$$

The forms of the plastic failure curves in Eq. (15d) are similar to those given in H Park and JY Kim [16], derived from the data given in ZP Bažant and PC Prat [9]. We modified these functions to have the new Eq. (15d).

For stability of the solution algorithm, the first-order derivatives of all quantities need to be finite across all values of plastic strains. Also, a property such that uniaxial or biaxial compression curves asymptotically tend to zero, unlike the hydrostatic curve [64], is also maintained in the principal compression coordinate system.

First, focusing on the hydrostatic curve, differentiating, substituting $\widetilde{e}_{p1} = \widehat{e}_{p1} - a$, and taking the limit $\widehat{e}_{p1} \rightarrow$ infinity, we obtain

$$\frac{\partial f_{p1}}{\partial \widehat{e}_{p1}} = c_{p1}(\frac{\widetilde{e}_{p1}}{a})^{-s}\frac{(sa + (1 - s)\widetilde{e}_{p1})}{\widetilde{e}_{p1}}$$

$$\lim_{\hat{e}_{p1}\rightarrow\infty}\frac{\partial f_{p1}}{\partial \widehat{e}_{p1}} = \lim_{\tilde{e}_{p1}\rightarrow\infty}\frac{\partial f_{p1}}{\partial \widehat{e}_{p1}} = c_{p1}(\frac{\widetilde{e}_{p1}}{a})^{-s}[\frac{sa}{\widetilde{e}_{p1}} + (1 - s)] = 0 \tag{C.4}$$

Proceeding similarly, when considering $\partial f_{pj}/\partial\widehat{e}_{pj}\rightarrow 0$ for increasing $\widehat{e}_{pj} \in (0, \infty]$ with $j = 2, 3$, all slopes of f_{pj} will be finite as the plastic strains accumulate, see Fig. 5(a). Actually, the values $\partial f_{pj}/\partial\widehat{e}_{pj}$ at $\widehat{e}_{pj} = 0$ are never encountered in the iteration with the finite increment Δe_j^p in Eq. (15b) giving $\widehat{e}_{pj} > 0$. Also, plastic flow is invoked only on loading of the material.

Second, focusing on the uniaxial and biaxial compression cases, proper strain location at maximum needs to be included in the coefficients. With $e_{pj}^c = 0$ in (C.1), solving for location of maximum f_{pj}^m for curve f_{pj} ($j = 2, 3$),

$$\frac{\partial f_{pj}}{\partial \widehat{e}_{pj}} = -\exp[-(\frac{\widehat{e}_{pj}}{c_j})^{m_j}]\left(m_j(\frac{\widehat{e}_{pj}}{c_j})^{m_j} - 1\right) = 0,$$

$$c_j = \frac{\widehat{e}_{pj}}{\exp[-(\frac{\ln m_j}{m_j})]} = \frac{\widehat{e}_{pj}}{m_j^{-1/m_j}} \tag{C.5}$$

and equating each $\widehat{e}_{pj}$ with the experimental values $\widehat{e}_{pj} = \widehat{\varepsilon}_{pj}$ in H Kupfer, HK Hilsdorf, and H Rusch [42], we arrive at $c_j = (\widehat{\varepsilon}_{pj})\cdot m_j^{(1/m_j)}$. The corresponding maximum value shown in Fig. 5(b-c) is

$$f_{pj}^{m} = f_{pj}\Big|_{\hat{e}_{pj}=\hat{\varepsilon}_{pj}} = \exp(-(m_j^{-1/m_2})^{m_2})(m_j^{-1/m_2})c_j \tag{C.6}$$

These strain locations are defined on the plastic counterpart instead of the elastic strain axes.

Finally, taking the limits of the constitutive matrix entries in Eq. (31c), we prove that the values are bounded

$$C_{IJ}^{ph} = \frac{E_I \widehat{e}_I^{p} E_J \widehat{e}_J^{p}}{\widehat{e}_1^{p} E_I \widehat{e}_1^{p} + \widehat{e}_2^{p} E_2 \widehat{e}_2^{p} + \widehat{e}_3^{p} E_3 \widehat{e}_3^{p}} \tag{C.7}$$

$$\lim_{\hat{e}_I^p \to \infty} C_{IJ}^{ph}\delta_{IJ} = E_I,\ \lim_{\hat{e}_I^p \to \infty} C_{IJ}^{ph} = 0\ I \neq J,\ \lim_{\hat{e}_I^p \to 0} C_{IJ}^{ph}\delta_{IJ} < E_I,\ \lim_{\hat{e}_I^p \to 0, \hat{e}_J^p \to 0} C_{IJ}^{ph} = 0\ I \neq J$$

Thus the system will be linearly solvable [34] with Eq. (31). Only 3 × 3 matrix solutions are needed in the flow iteration in Eq. (29b) and plastic constitutive matrix in Eq. (31c).

Data availability

Data will be made available on request.

References

[1] Bathe KJ, Ramaswamy S. On three-dimensional nonlinear analysis of concrete structures. Nucl Eng Des 1979;52(3):385–409.

[2] Bathe KJ, Walczak J, Welch A, Mistry N. Nonlinear analysis of concrete structures. Comput Struct 1989;32(3–4):563–90.

[3] Argyris JH, Faust G, Szimmat J, Warnke EP, Willam KJ. Recent developments in the finite element analysis of prestressed concrete reactor vessels. Nucl Eng Des 1974;28(1):42–75.

[4] Seible F, Scordelis AC. Nonlinear analysis of multi-cell reinforced concrete box girder bridges. Eng Struct 1983;5(1):45–57.

[5] Meyer C, Bathe KJ. Nonlinear analysis of R/C structures in practice. J Struct Div 1982;108(7):1605–22.

[6] Bažant ZP, Kim SS. Plastic-fracturing theory for concrete. J Eng Mech Div 1979;105 (3):407–28.

[7] Hsieh SS, Ting EC, Chen WF. A plastic-fracture model for concrete. Int J Solids Struct 1982;18(3):181–97.

[8] Lee J, Fenves GL. Plastic-damage model for cyclic loading of concrete structures. J Eng Mech 1998;124(8):892–900.

[9] Bažant ZP, Xiang Y, Prat PC. Microplane model for concrete. I: Stress-strain boundaries and finite strain. J Eng Mech 1996;122(3):245–54.

[10] Bažant ZP, Adley MD, Carol I, Jirásek M, Akers SA, Rohani B, et al. Large-strain generalization of microplane model for concrete and application. J Eng Mech 2000; 126(9):971–80.

[11] Kuhl E, Ramm E. Micro plane modeling of cohesive frictional materials. Eur J Mech A/Solids 2000;19:S121–43.

[12] Peyman F, Sadrnejad SA. Analysis of concrete crack growth based on micro-plane model. Struct Concr 2018;19(3):930–45.

[13] "A thermodynamically consistent approach to micro plane theory. Part I: Free energy and consistent micro plane stresses." Int. J. Solids & Structures, 38, 2921-2931, 2001.

[14] Cusatis G, Bažant ZP, Cedolin L. Confinement-shear lattice model for concrete damage in tension and compression: I. Theory. J Eng Mech 2003;129(12):1439–48.

[15] Grassl P. A lattice approach to model flow in cracked concrete. Cem Concr Compos 2009;31(7):454–60.

[16] Park H, Kim JY. Plasticity model using multiple failure criteria for concrete in compression. Int J Solids Struct 2005;42(8):2303–22.

[17] Park HG, Klingner RE. Nonlinear analysis of RC members using plasticity with multiple failure criteria. J Struct Eng 1997;123(5):643–51.

[18] Park H, Kim JY. Hybrid plasticity model for reinforced concrete in cyclic shear. Eng Struct 2005;27(1):35–48.

[19] Pirmoradi P, Suiker AS, Poorsolhjouy P. Multi-scale constitutive model for fiber-reinforced concrete with FEM analyses of structural failure. Eng Fract Mech 2025; 111166.

[20] Grande E, Imbimbo M, Milani G, Tomei V. A 1D-finite element framework for analyzing the cyclic bond response of FRP-strengthened concrete elements. In *Structures* (2025, September) (Vol. 79, p. 109615). Elsevier.

[21] Jirásek M, Grassl P. Evaluation of directional mesh bias in concrete fracture simulations using continuum damage models. Eng Fract Mech 2008;75(8): 1921–43.

[22] Bažant ZP, Jirásek M. Nonlocal integral formulations of plasticity and damage: survey of progress. J Eng Mech 2002;128(11):1119–49.

[23] Gonçalves GF, Lopes IAR, Carneiro AMC, Pires FMA. A critical comparison of gradient and integral nonlocal damage models: formulation, numerical predictions and computational aspects. Finite Elem Anal Des 2025;248:104358.

[24] Wosatko A, Genikomsou A, Pamin J, Polak MA, Winnicki A. Examination of two regularized damage-plasticity models for concrete with regard to crack closing. Eng Fract Mech 2018;194:190–211.

[25] Al-Rub RA, Voyiadjis GZ. A direct finite element implementation of the gradient-dependent theory. Int J Numer Meth Eng 2005;63(4):603–29.

[26] Jouan G, Kotronis P, Collin F. Using a second gradient model to simulate the behaviour of concrete structural elements. Finite Elem Anal Des 2014;90:50–60.

[27] Zreid I, Kaliske M. A gradient enhanced plasticity–damage microplane model for concrete. Comput Mech 2018;62(5):1239–57.

[28] Ahmed A, Liu Y, Tafsirojjaman T, Ahmad A, Iqbal M. Phase field model for mixed mode fracture in concrete. Eng Fract Mech 2023;289:109439.

[29] Živković J, Dunić V, Milovanović V, Pavlović A, Živković M. A modified phase-field damage model for metal plasticity at finite strains: Numerical development and experimental validation. Metals 2020;11(1):47.

[30] Bažant ZP, Oh BH. Crack band theory for fracture of concrete. Matériaux et construction 1983;16(3):155–77.

[31] Kotsovos MD, Pavlović MN. Structural concrete: finite-element analysis for limit-state design. Thomas Telford; 1995.

[32] Červenka J, Papanikolaou VK. Three dimensional combined fracture–plastic material model for concrete. Int J Plast 2008;24(12):2192–220.

[33] Kojic M, Bathe KJ. Inelastic analysis of solids and structures. Berlin: Springer; 2005.

[34] Bathe KJ. Finite element procedures. Prentice Hall; 1996, 2nd ed. K.J. Bathe, Watertown, MA; 2014 and Higher Education Press, China; 2016. Springer-Verlag, in press.

[35] Bathe KJ. Finite Element Procedures – En Plus. Springer Verlag, in press.

[36] Bathe KJ, Dvorkin EN. On the automatic solution of nonlinear finite element equations. Comput Struct 1983;17(5–6):871–9.

[37] Bathe KJ. The AMORE paradigm for finite element analysis. Adv Eng Softw 2019; 130:1–13.

[38] Bucalem ML, Bathe KJ. The mechanics of solids and structures-hierarchical modeling and the finite element solution. Springer Science & Business Media; 2011.

[39] Kotsovos MD, Newman JB. Generalized stress-strain relations for concrete. J Eng Mech Div 1978;104(4):845–56.

[40] Launay P, Gachon H. Strain and ultimate strength of concrete under triaxial stress. Special Publication 1972;34:269–82.

[41] Wang CZ, Guo ZH, Zhang XQ. An experimental investigation of biaxial and triaxial compressive concrete strength and deformation. 1987, August. In Transaction of 9th International Conference on Structural Mechanics in Reactor Technology. Lausanne Aug (pp. 193-198).

[42] Kupfer H, Hilsdorf HK, Rusch H. Behavior of concrete under biaxial stresses. 1969, August. In Journal proceedings (Vol. 66, No. 8, pp. 656-666).

[43] Green SJ, Swanson SR. Static constitutive relations for concrete, 1973. In: Air Force Weapons Lab. Tech. Rep., AFWL-TR-72-244, Kirtland Air Force Base, Albuquerque, N. Mex.

[44] Menetrey P, Willam KJ. Triaxial failure criterion for concrete and its generalization. Struct J 1995;92(3):311–8.

[45] Jirásek M, Bauer M. Numerical aspects of the crack band approach. Comput Struct 2012;110:60–78.

[46] Theory and Modeling Guide Volume 1:ADINA, Bentley Systems, Inc., ADINA 25.00.01, Section 3.7, 2025.

[47] Desayi P, Krishnan S. Equation for the stress-strain curve of concrete. 1964, March. In Journal Proceedings (Vol. 61, No. 3, pp. 345-350).

[48] Cervenka V, Gerstle KH. Inelastic analysis of reinforced concrete panels. Theory, Publ Int Assoc Bridge Struc Eng 1971;31:31–45.

[49] Darwin D, Pecknold DA. Analysis of RC shear panels under cyclic loading. J Struct Div 1976;102(2):355–69.

[50] Kwak HG, Kim DY. Nonlinear analysis of RC shear walls considering tension-stiffening effect. Comput Struct 2001;79(5):499–517.

[51] Bresler B, Scordelis AC. Shear strength of reinforced concrete beams. 1963, January. In Journal Proceedings (Vol. 60, No. 1, pp. 51-74).

[52] Vecchio FJ. Analysis of shear-critical reinforced concrete beams. ACI Struct J 2000; 97(1):102–10.

[53] Kormeling HA, Reinhardt HW. Determination of the fracture energy of normal concrete and epoxy modified concrete. Tech. rep. 5-83-18, Stevin Lab, Delft University of Technology; 1983.

[54] Carol I, Prat PC. Smeared analysis of concrete fracture using a microplane based multicrack model with static constraints. In: van Mier JGM, Rots JG, Bakker A, editors. Fracture processes in concrete, rock and ceramics. Noordwijk (The Netherlands): E&FN Spon; 1991. p. 619–28.

[55] Lotfi HR, Shing PB. Embedded representation of fracture in concrete with mixed finite elements. Int J Numer Meth Eng 1995;38:1307–25.

[56] Bobinski J, Tejchman J. Modelling of concrete behaviour with a non-local continuum damage approach. Arch Hydro-Eng Environ Mech 2005;52:243–63.

[57] Prasad MVKV, Krishnamoorthy CS. Computational model for discrete crack growth in plain and reinforced concrete. Comput Methods Appl Mech Eng 2002;191: 2699–725.

[58] Ko Y, Lee PS, Bathe KJ. A new MITC4+ shell element. Comput Struct 2017;182: 404–18.

[59] Ko Y, Bathe KJ, Zhang X. Continuum mechanics-based shell elements with six degrees of freedom at each node− the MITC4/D and MITC4+/D elements. Comput Struct 2025;308:107622.

[60] Carpinteri A, Valente S, Ferrara G, Imperato L. Experimental and numerical fracture modelling of a gravity dam. In: Fracture mechanics of concrete structures. CRC Press; 2003. p. 351–60.

[61] Mukhtar F, El-Tohfa A. A review on fracture propagation in concrete: Models, methods, and benchmark tests. Eng Fract Mech 2023;281:109100.

[62] Gálvez JC, Červenka J, Cendón DA, Saouma V. A discrete crack approach to normal/shear cracking of concrete. Cem Concr Res 2002;32(10):1567–85.

[63] Tambusay A, Suprobo P, Suryanto B, Don W. Application of nonlinear finite element analysis on shear-critical reinforced concrete beams. J Eng Technol Sci 2021;53(4):210408.

[64] Lubliner J, Oliver J, Oller S, Onate E. A plastic-damage model for concrete. Int J Solids Struct 1989;25(3):299–326.

[65] Morgan SP, Johnson CA, Einstein HH. Cracking processes in Barre granite: fracture process zones and crack coalescence. Int J Fract 2013;180(2):177–204.